International Journal of Mechanical Sciences 165 (2020) 105196

Contents lists available at ScienceDirect

International Journal of Mechanical Sciences

journal homepage: www.elsevier.com/locate/ijmecsci

Single-fiber pull-out analysis comparing the intensities of singular stress fields (ISSFs) at fiber end/entry points

Nao-Aki Noda, Dong Chen*, Guowei Zhang, Yoshikazu Sano

Department of Mechanical Engineering, Kyushu Institute of Technology, Tobata-Ku, Kitakyushu-city, Fukuoka, 804-8550, Japan

A R T I C L E I N F O

Keywords:
Fiber-pullout
Partially-embedded
Fiber/matrix interface
Intensity of singular stress field (ISSF)
Finite element method (FEM)
Body force method (BFM)

A B S T R A C T

This paper deals with a partially-embedded single-fiber under pull-out force in comparison with a single fiber embedded in matrix focusing on two distinct singular stress fields. Then, the intensities of the singular stress fields (ISSFs) are compared at the fiber end named Point A and the fiber/surface intersection named Point E. The results show that if the embedded length l_{in} is shorter, interface debonding may occur at Point A. Instead, if l_{in} is longer, the interface debonding may occur at Point E. To analyze the ISSFs accurately, a mesh-independent technique coupled with the finite element method (FEM) is indicated by applying the same FEM mesh pattern to the pull-out model and the reference model. As the reference solution, a single fiber embedded in matrix is also calculated under arbitrary material combinations by using the body force method (BFM). Stress distributions along the fiber/matrix interfaces are also calculated for carbon and glass fibers.

1. Introduction

Wide application of fiber composite technology in various fields is based on taking advantage of the high strength and high stiffness of fibers. In fiber composites, both the fiber and the matrix retain their original physical and chemical identities, yet together they produce a combination of mechanical properties that cannot be achieved with either of the constituents acting alone [1,2].

Many different alternative test set-ups and experimental techniques have been developed in recent years to gain more insight into the basic mechanisms, dominating the properties of the fiber/matrix interface. One of the most popular is the pull-out test as shown in Fig. 1, where a single fiber or bar partially embedded in resin is pulled out from the surrounding matrix and the corresponding relation between load $P(\delta)$ and displacement δ is recorded [3]. Typical relation between the pull-out load vs. displacement contains three typical zones, that is, linear elastic zone, crack extension zone and fiber extruding zone [4].

Such debonding test or pull-out test has been used as an advantageous micromechanical test used to characterize interfacial fiber/matrix bonding. To pull out the fiber, since the debonding strength should be smaller than the tensile strength of the fiber, high adhesion systems require very small embedding lengths l_{in} (<100 μm) [2]. The small embedding lengths sometimes make the test unusable because the pull-out force has to break the adhesion at the fiber end. The effect of the embedded length on the debonding stress at the fiber end should be clarified especially in the range of short embedded length around $l_{in} = 5D$.

Fig. 1 shows a two-dimensional single fiber partially embedded considered in this study. The shaded (slashed) part represents a rectangular-shaped fiber whose Young's modulus is denoted by E_F and whose Poisson's Ratio is denoted by ν_F. The grey portion represents the matrix having a semi-infinite region whose Young's modulus is denoted by E_M and whose Poisson's Ratio is denoted by ν_M. Subscripts M, F represent the matrix and reinforcing fiber, respectively. Assume that perfectly bonded fiber/matrix interface whose material properties vary in a stepwise manner across the interface. A uniform tensile stress is distributed at the free end of the fiber, and the total force is P. The embedding length l_{in} represents the distance from the surface of the matrix to the buried end of fiber. Notation D represents the diameter of the fiber, i.e. the width of the fiber in this 2D analysis. Point E is used to represents the interface on the surface of the matrix. Similarly, Point A represents the interface corner at the fiber end. Notations E_F, ν_F, E_M, ν_M represent the Young's modulus and Poisson's ratio of fiber and matrix, respectively. Singular interface stress fields [5–7], which will be explained in the next section, are indicated in Fig. 1 around Point A and Point E. They are controlled by the intensity of the singular stress fields (ISSFs, denoted by $K^{A}_{\sigma,\lambda_1^A}$ etc.) [5–7].

Many researchers have been working on fiber pull-out experiments. For example, Scheer et al. [8] experimentally investigated interfacial peeling of reinforcing fibers, focusing on the energy release rate. Zhandarov et al. [9,10] investigated the pull-out force versus displacement. The $P(\delta)$ curve of pull-out test and $P(\delta)$ curve of micro-bond tests is similar, i.e. crack propagation may starts from the fiber entry Point E [8–10]. Marotzke C. et al. [11] investigated the influence of thermally induced

* Corresponding author.
E-mail address: shumadong@gmail.com (D. Chen).

https://doi.org/10.1016/j.ijmecsci.2019.105196
Received 11 August 2019; Received in revised form 25 September 2019; Accepted 27 September 2019
Available online 28 September 2019

Nomenclature

FEM	Finite element method
ISSF	Intensity of singular stress field
BFM	Body force method
RWCIM	Reciprocal work contour integral method
Point A	Fiber buried end
Point E	Fiber intersection on the surface of the matrix
E, E_F, E_M	Young's modulus
ν, ν_F, ν_M	Young's modulus
G, G_F, G_M	Shear modulus
K, K_{I}, K_{II}, K_σ, K_τ	Intensity of singular stress field (ISSF)
F, F_{I}, F_{II}	Dimensionless ISSF
σ_x, σ_y	Tension or compression stress
τ	Shear stress
l	Fiber length
l_{in}	Fiber embedding length
D	Width of the fiber
σ_∞	Tension stress on the boundary of infinite plate
P	Pull-force on the free end of fiber
α, β	Dundurs' material composite parameters
λ, λ_1^A, λ_2^A, λ_1^E, λ_2^E	Singular index
e_{min}	Minimum element size in FEM
r_1, r_2, r_3	Distance from Point A or Point E along the interface

Subscripts

F	Fiber
M	Matrix
FEM	Corresponding values in FEM analysis
I	Mode I deformation
II	Mode II deformation
A	Corresponding values at Point A
E	Corresponding values at Point E
*	Corresponding values in reference model

stresses and interfacial friction on the interfacial debonding process, focusing on the energy release rate. Wang C et al. [12] and K.-H. Tsai et al. [13] investigated the process of fiber pull-out test, focusing on peeling and friction slip, it is observed that crack initiate at the fiber bonded end Point A during the fiber pull-out test [12,13]. In a rod pull out test that very similar to fiber pull-out test, Atkinson, et al. [14] observed crack initiation sometimes occur at Point A and sometimes occur at Point E in Fig. 1.

In the previous pull-out experiments, the interface strength was discussed between the fiber and the matrix without paying attention to the intensity of singular stress field (ISSF). As shown in Fig. 1, however, due to the singular stress fields crack initiation sometimes occurs at Point A, sometimes occur at Point E. Then, the crack may propagate causing final failure. Therefore, to evaluate the mechanical strength of the composites, it is necessary to know the ISSFs at these two points. In the previous studies, the shear-lag theory was widely used to discuss the shear stress distribution of the fiber interface. However, this theory is simply based on one-dimensional fiber model assuming the fiber interface transmits only the shear stress [15–17]; and therefore, this theory cannot express the singular stress fields. In other words, a lot of analytical studies have been done to clarify pull-out phenomena [18–20], but no studies are available for the ISSF.

The authors' recent studies have shown that the ISSFs are useful for evaluating the interface strength because they control the adhesive strength for butt and lap joints [21–27]. Therefore, this paper will focus on the ISSFs of a single fiber partially embedded in a matrix under pull out force. Then, the effect of fiber embedded length on the ISSFs will be investigated and the severities at the fiber end Point A and at the fiber entry Point E will be compared by considering their fiber interface stress distributions. The final goal of this study is to clarify the fiber pull out mechanism toward designing suitable fiber reinforced composites.

2. Singular stress fields and the ISSF at the fiber end

In this study the finite element method (FEM) is applied to calculating the ISSFs. Since the FEM stress values are usually affected by the mesh size, in the previous study [28,29] the same mesh pattern is applied around the singular points for unknown and reference problems. Then, it was found that the FEM stress ratio of the unknown and reference problem is constant independent of the mesh size. Therefore, the FEM stress ratio is equal to the ISSF ratio because the FEM mesh error can be eliminated by considering FEM stress ratio and applying the same mesh (Detail is discussed in Tables 2a and 2b). By choosing the reference problem as an exact solution available, the ISSF of the unknown problem can be obtained by multiplying the FEM stress ratio and the

$$\begin{cases} \sigma_y^A(r_1) = \dfrac{K^A_{\sigma,\lambda_1^A}}{r_1^{\,1-\lambda_1^A}} + \dfrac{K^A_{\sigma,\lambda_2^A}}{r_1^{\,1-\lambda_2^A}} \\ \tau_{yx}^A(r_1) = \dfrac{K^A_{\tau,\lambda_1^A}}{r_1^{\,1-\lambda_1^A}} + \dfrac{K^A_{\tau,\lambda_2^A}}{r_1^{\,1-\lambda_2^A}} \end{cases} \qquad \begin{cases} \sigma_x^A(r_2) = \dfrac{K^A_{\sigma,\lambda_1^A}}{r_2^{\,1-\lambda_1^A}} - \dfrac{K^A_{\sigma,\lambda_2^A}}{r_2^{\,1-\lambda_2^A}} \\ \tau_{xy}^A(r_2) = \dfrac{K^A_{\tau,\lambda_1^A}}{r_2^{\,1-\lambda_1^A}} - \dfrac{K^A_{\tau,\lambda_2^A}}{r_2^{\,1-\lambda_2^A}} \end{cases}$$

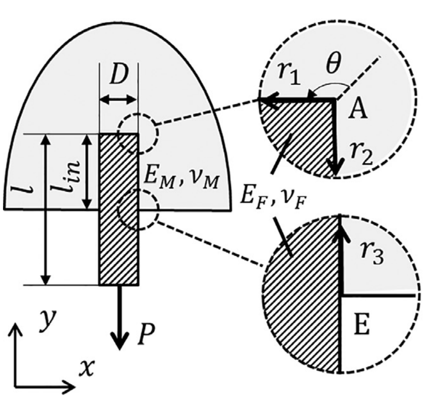

$$\begin{cases} \sigma_x^E(r_3) = \dfrac{K^E_{\sigma,\lambda_1^E}}{r_3^{\,1-\lambda_1^E}} + \dfrac{K^E_{\sigma,\lambda_2^E}}{r_3^{\,1-\lambda_2^E}} \\ \tau_{xy}^E(r_3) = \dfrac{K^E_{\tau,\lambda_1^E}}{r_3^{\,1-\lambda_1^E}} + \dfrac{K^E_{\tau,\lambda_2^E}}{r_3^{\,1-\lambda_2^E}} \end{cases}$$

Fig. 1. Two-dimensional pull-out model for partially embedded fiber with the singular stress fields along the local coordinates r_1, r_2, r_3. The intensities of the singular stress fields (ISSFs) are denoted by K^A_{σ,λ_1^A} etc. [5–7].

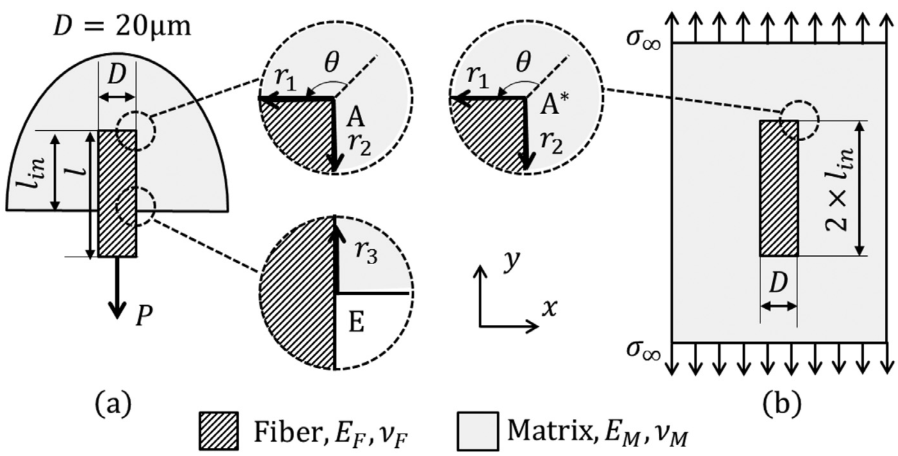

Fig. 2. 2D modelling: (a) a single rectangular fiber pull-out from a semi-infinite plate; (b) a single rectangular fiber in an infinite plate under remote tension used as the reference solution.

Table 1
Mechanical properties.

Fiber/Matrix	(a): Carbon Fiber/ Epoxy	(b): Glass Fiber/ Epoxy
E_F(GPa)	276	75
E_M(GPa)	3.03	3.3
ν_F	0.30	0.17
ν_M	0.35	0.35
α	0.9775	0.9071
β	0.2250	0.2016
λ_1^A	0.7784	0.7632
λ_2^A	0.6158	0.6218
λ_1^E	0.6751	0.6592
λ_2^E	0.9999	0.9992
D(μm)	20	20
l_{in}(μm)	100	100
Crack initiation	Point A	Point A

ISSF of the exact solution. Regarding fiber end Point A, a single fiber in an infinite plate can be chosen as the reference problem. The analysis method used in this study can be called the proportional method since the method is based on the proportional FEM stress fields [30–35]. This mesh-independent technique is a convenient ISSF calculation method, and the obtained ISSFs are denoted by $K^A_{\sigma,\ \lambda_1^A}$ etc. [5–7].

Fig. 1 shows the two-dimensional model of fiber pull-out problem considered in this paper. Here, a 2D rectangular shape is used to represent the fiber focusing on the singular stress fields at Point A and Point E. Although cylindrical shape may be more suitable for representing the fiber, the non-singular term caused by the circumferential strain must be removed and the analysis becomes complicated [24,25]. Therefore, this modelling should be considered after considering the rectangular modelling.

Table 1 shows mechanical properties of the Fiber/Matrix considered in this study. The base material Epon 828 can be obtained by curing a bisphenol A type liquid epoxy resin with m-phenylenediamine. In the previous study, for example, a pull-out test was conducted for a single glass-fiber whose diameter $D = 21\mu$m from the matrix Epon 828 [28]. Since the aspect ratio l_{in}/D mainly controls the pull-out behavior, $D = 20\mu$m is assumed as shown in Table 1 and Fig. 2. Here, l denotes the total fiber length and l_{in} the denotes the embedded length; then, $l_{in}/D = 5$ means $l_{in} = 100\mu$m. To obtain the ISSF at the fiber end, model as shown in Fig. 2(b) is used as a reference problem. This is because the exact solution is available for the problem as shown in Fig. 2(b) [5,36–38], which is a rectangular fiber fully embedded in an infinite plate and the total length of the fiber is $2l_{in}$. Symbol σ_∞ in Fig. 2 denotes the uniform tensile stress on the boundary of the infinite plate.

In this study, the ISSFs at Point A and Point E, for the problem as shown in Fig. 1, are mainly discussed by varying l_{in}. Then, the x-y coordinate system as shown in Fig. 1 is used. The y-direction corresponds to the axial direction of the fiber, and the x-direction corresponds to the radial direction of the fiber. Notation r_1 denotes the distance from Point A in the x-direction, and r_2 denotes the distance from Point A in the y-direction. Then, $r_1 = 0$ and $r_2 = 0$ means Point A. Notation r_3 denotes the distance from Point E in the y-direction, and $r_3 = 0$ represents Point E.

Note that the singular stress field at Point A in Fig. 2(a) is similar to the singular stress field at Point A* of the reinforcing fiber in the matrix shown in Fig. 2(b). The ISSF of Point A* in Fig. 2(b) can be calculated by the body force method (BFM) [5,36–38]. The BFM is a powerful analytical method to obtain accurate solutions, which can be virtually regarded as exact solutions.

Till recently, a lot of studies have considered Dundurs' composite parameters of typical engineering materials. Suga et al. investigated the parameters and mechanical compatibility of various material joints [39]. Yuuki [40] showed the variations of the parameters in the $\alpha - \beta$ space for the materials combinations among metal, ceramics, resin, and glass. Here, α, β denote Dundurs bimaterial parameters [41] defined by equation (A.1) in Appendix A. In this study, analysis is carried out under plane strain assumption. Singular indexes λ_1^A and λ_2^A at the corner A can be calculated by solving equations (A.2a) and (A.2b), respectively [36,42]. For the material combination Carbon Fiber/Epoxy in Table 1(a), $\alpha = 0.9775$, $\beta = 0.2250$), $\lambda_1^A = 0.7784$ and $\lambda_2^A = 0.6158$.

The ISSF at Point A* in Fig. 2(b) was discussed in [5,37,42]. It should be noted that Eqs. (1) and (2) [28,42] express the singular stress at Point A* in Fig. 2(b) and also Point A in Fig. 2(a). Here, K^A_{σ,λ_1^A}, K^A_{σ,λ_2^A} denote ISSFs for normal stress at Point A and K^A_{τ,λ_1^A} and K^A_{τ,λ_2^A} denote ISSFs for shear stress. ISSFs K^A_{σ,λ_1^A} and K^A_{τ,λ_1^A} correspond to Mode I deformation and ISSFs K^A_{σ,λ_2^A} and K^A_{τ,λ_2^A} correspond to Mode II deformation.

$$\begin{cases} \sigma_y^A(r_1) = \dfrac{K^A_{\sigma,\ \lambda_1^A}}{{r_1}^{1-\lambda_1^A}} + \dfrac{K^A_{\sigma,\ \lambda_2^A}}{{r_1}^{1-\lambda_2^A}} \\ \tau_{yx}^A(r_1) = \dfrac{K^A_{\tau,\ \lambda_1^A}}{{r_1}^{1-\lambda_1^A}} + \dfrac{K^A_{\tau,\ \lambda_2^A}}{{r_1}^{1-\lambda_2^A}} \end{cases} \tag{1}$$

$$\begin{cases} \sigma_x^A(r_2) = \dfrac{K^A_{\sigma,\ \lambda_1^A}}{{r_2}^{1-\lambda_1^A}} - \dfrac{K^A_{\sigma,\ \lambda_2^A}}{{r_2}^{1-\lambda_2^A}} \\ \tau_{xy}^A(r_2) = \dfrac{K^A_{\tau,\ \lambda_1^A}}{{r_2}^{1-\lambda_1^A}} - \dfrac{K^A_{\tau,\ \lambda_2^A}}{{r_2}^{1-\lambda_2^A}} \end{cases} \tag{2}$$

For the singular stress field at Point A, the interface corner of different materials, the indexes of the singular stress field are different depending on the mode I and mode II deformation [5]. In order to de-

Table 2a
FEM Stress ratio of symmetrical type with $\lambda_1^A = 0.7784$ when $l_{in} = 100\mu$m in Fig. 2(a) and $l_{in} = 500\mu$m in Fig. 2(b) for the material combination in Table 1(a).

Smallest mesh size $e_{min} = 3^{-9}$ [mm]			Smallest mesh size $e_{min} = 3^{-10}$ [mm]		
$\frac{r}{e_{min}}$	$\sigma^{A}_{I,\ FEM}(r)$ [MPa]	$\frac{\sigma^{A}_{I,\ FEM}(r)}{\sigma^{A*}_{I,\ FEM}(r)}$	$\frac{r}{e_{min}}$	$\sigma^{A}_{I,\ FEM}(r)$ [MPa]	$\frac{\sigma^{A}_{I,\ FEM}(r)}{\sigma^{A*}_{I,\ FEM}(r)}$
0.0	1.290	0.117	0.0	1.647	0.117
0.5	1.038	0.117	0.5	1.328	0.117
1.0	0.779	0.116	1.0	0.998	0.117
1.5	0.699	0.116	1.5	0.896	0.116
2.0	0.692	0.115	2.0	0.889	0.116

Table 2b
FEM stress ratio of skew-symmetrical type with $\lambda_2^A = 0.6158$ when $l_{in} = 100\mu$m in Fig. 2(a) and $l_{in} = 500\mu$m in Fig. 2(b) for the material combination in Table 1(a).

Smallest mesh size $e_{min} = 3^{-9}$ [mm]			Smallest mesh size $e_{min} = 3^{-10}$ [mm]		
$\frac{r}{e_{min}}$	$\sigma^{A}_{II,\ FEM}(r_1)$ [MPa]	$\frac{\sigma^{A}_{II,\ FEM}(r_1)}{\sigma^{A*}_{II,\ FEM}(r_1)}$	$\frac{r}{e_{min}}$	$\sigma^{A}_{II,\ FEM}(r_1)$ [MPa]	$\frac{\sigma^{A}_{II,\ FEM}(r_1)}{\sigma^{A*}_{II,\ FEM}(r_1)}$
0.0	10.161	0.104	0.00	15.497	0.104
0.5	4.279	0.104	0.5	6.524	0.104
1.0	1.821	0.104	1.0	2.773	0.104
1.5	2.913	0.104	1.5	4.438	0.104
2.0	3.048	0.104	2.0	4.642	0.104

termine the ISSFs, it is necessary to consider the two distinct mode I and mode II singular stress fields at the same time. The shear stress along the interface of fiber and matrix has been widely discussed by using the shear-lag theory [8,10,15–17], which is simply based on a one-dimensional model and cannot express singular stress fields.

At the vicinity of Point A, the stress distribution corresponding to Mode I deformation is denoted by $\sigma_I^A(r)$, as shown in Eq. (3). It is proportional to $1/r^{1-\lambda_1^A}$. And the stress distribution corresponding to Mode II deformation, denoted by $\sigma_{II}^A(r)$, is proportional to $1/r^{1-\lambda_2^A}$. These singular stress fields together determine the stress distributions along the interfaces near Point A. Each ISSF can be defined as parameters $K^A_{I,\ \lambda_1^A}$ and $K^A_{II,\ \lambda_2^A}$ as shown in Eq. (4). In this equation, we can put $r = r_1 = r_2$.

$$\begin{cases} 2\sigma_I^A(r) = \sigma_y^A(r_1) + \sigma_x^A(r_2) \\ 2\sigma_{II}^A(r) = \sigma_y^A(r_1) - \sigma_x^A(r_2) \end{cases} (r = r_1 = r_2) \tag{3}$$

$$\begin{cases} K^A_{I,\lambda_1^A} = \lim\limits_{r\to 0}\left[\sigma_I^A(r)\cdot r^{1-\lambda_1^A}\right] \\ K^A_{II,\lambda_2^A} = \lim\limits_{r\to 0}\left[\sigma_{II}^A(r)\cdot r^{1-\lambda_2^A}\right] \end{cases} \tag{4}$$

The ISSFs K^A_{σ,λ_1^A} and K^A_{τ,λ_1^A} in Eq. (1) can be determined from the ISSF K^A_{I,λ_1^A}. For Fig. 2, the ISSFs K^A_{σ,λ_1^A} and K^A_{τ,λ_1^A} are proportional to K^A_{I,λ_1^A} and the ISSFs K^A_{σ,λ_2^A} and K^A_{τ,λ_2^A} are proportional to K^A_{II,λ_2^A}.

The normalized stress intensity factors F_I^* and F_{II}^* can be acquired on the basis of BFM [37–42]. And the definition of F_I^* and F_{II}^* of the reference problem were expressed as shown in Eq. (5) [37], in which $\sigma_\infty = 1$ is tension stress at the boundary of the infinite matrix, as shown in Fig. 2(b).

$$\begin{cases} F_I^* = K^*_{I,\lambda_1^A} / \left[\sigma_\infty\sqrt{\pi}(D/2)^{1-\lambda_1^A}\right] \\ F_{II}^* = K^*_{II,\lambda_2^A} / \left[\sigma_\infty\sqrt{\pi}(D/2)^{1-\lambda_2^A}\right] \end{cases} \tag{5}$$

Therefore, the normalized stress intensity factors of the fiber pull-out problem, as shown in Fig. 2(a), are defined similarly as follows:

$$\begin{cases} F_I = K^A_{I,\lambda_1^A} / \left[(P/D)\sqrt{\pi}(D/2)^{1-\lambda_1^A}\right] \\ F_{II} = K^A_{II,\lambda_2^A} / \left[(P/D)\sqrt{\pi}(D/2)^{1-\lambda_2^A}\right] \end{cases} \tag{6}$$

By using the proportional method [30–35] mentioned above, F_I and F_{II} for the pull-out problem can be calculated from the ISSFs $F_I^*$and $F_{II}^*$of the reference problem. As is shown in Eq. (7). Here, $\sigma^A_{I,\ FEM}(r)$ and $\sigma^{A*}_{I,\ FEM}(r)$ represent the stress distributions corresponding to Mode I deformation in FEM analysis as mentioned above. Similarly, $\sigma^A_{II,\ FEM}(r)$ and $\sigma^{A*}_{II,\ FEM}(r)$ correspond to Mode II deformation.

$$\frac{F_I}{F_I^*} = \frac{\sigma^A_{I,\ FEM}(r)}{\sigma^{A*}_{I,\ FEM}(r)},\ \frac{F_{II}}{F_{II}^*} = \frac{\sigma^A_{II,\ FEM}(r)}{\sigma^{A*}_{II,\ FEM}(r)}. \tag{7}$$

The Finite Element Method (FEM) has been widely used for many engineering applications [43–45]. Regarding fiber reinforced composite analyses, Stern et al. [46] developed a path independent integral formula for the computation of the intensity of the stress singularity by using FEM. Atkinson et al. [14], Povirk et al. [20], and Freund et al. [47] conducted fiber pullout simulation studies by using a circular rigid cylinder. Hann et al. [48] investigated the effect of contact angle, loading position and loading type in micro-bond test by using FEM. Ash et al. [49] investigated the effect of bead geometry and knife angle in micro-bond test via FEM. Zhang et al. [50] studied the effects of interfacial debonding and sliding on fracture characterization of unidirectional fibre-reinforced composites by using FEM. Brito-Santana et al. [51] studied influence of the debonding between fiber and matrix in micro scale via the FEM. FEM is widely used in studies in fiber reinforced composites [52–58]. Ahmed et al. [59–63] studied sensing, low loss and birefringent etc. by using FEM. In this analysis software MSC Marc is used to express the pull-out model for Figs. 1 and 2(a), and the reference model for Fig. 2(b). Stress distributions along the interfaces (r_1, r_2) are calculated by applying the same mesh pattern to the pull-out model and reference model. Thus stress ratio[$\sigma^A_{I,\ FEM}(r)/\sigma^{A*}_{I,\ FEM}(r)$] and [$\sigma^A_{II,\ FEM}(r)/\sigma^{A*}_{II,\ FEM}(r)$] can be calculated between the pull-out model and the reference model. This method was used in [23–29].

As is shown in Eq. (3), $\sigma^A_{I,\ FEM}(r)$ is calculated from the stress distributions $\sigma_y^A(r_1)$ along the interface r_1 and $\sigma_x^A(r_2)$ along the interface r_2 by using the pull-out model (Fig. 2(a)). Similarly, $\sigma^{A*}_{I,\ FEM}(r)$ is calculated from the stress distributions $\sigma_y^{A*}(r_1)$ along the interface r_1 and $\sigma_x^{A*}(r_2)$ along the interface r_2 by using the reference model (Fig. 2(b)). Material

Table 3a
FEM stress ratio of the first term with $\lambda_1^E = 0.6751$ when $l_{in} = 100\mu$m and $l_{in} = 200\mu$m in Fig. 1(a) for the material combination in Table 1(a).

Smallest mesh size $e_{min} = 3^{-9}$ [mm]			Smallest mesh size $e_{min} = 3^{-10}$ [mm]			RWCIM
$\frac{r}{e_{min}}$	$\sigma^E_{FEM,\lambda_1}(r)$ [MPa]	$\frac{\sigma^E_{FEM,\lambda_1}(r)}{\sigma^{E*}_{FEM,\lambda_1}(r)}$	$\frac{r}{e_{min}}$	$\sigma^E_{FEM,\lambda_1}(r)$ [MPa]	$\frac{\sigma^E_{FEM,\lambda_1}(r)}{\sigma^{E*}_{FEM,\lambda_1}(r)}$	$\frac{K^E_{\sigma,\lambda_1}}{K^{E*}_{\sigma,\lambda_1}}$
0.0	13.022	1.34	0.0	9.114	1.34	
0.5	11.102	1.34	0.5	7.770	1.34	
1.0	8.131	1.34	1.0	5.691	1.34	1.34
1.5	6.775	1.34	1.5	4.742	1.34	
2.0	6.389	1.34	2.0	4.472	1.34	

Table 3b
FEM stress ratio of the second term with $\lambda_2^E = 0.9999$ when $l_{in} = 100\mu$m and $l_{in} = 200\mu$m in Fig. 1(a) for the material combination in Table 1(a).

Smallest mesh size $e_{min} = 3^{-9}$ [mm]			Smallest mesh size $e_{min} = 3^{-10}$ [mm]			RWCIM
$\frac{r}{e_{min}}$	$\sigma^E_{FEM,\lambda_2}(r)$ [MPa]	$\frac{\sigma^E_{FEM,\lambda_2}(r)}{\sigma^{E*}_{FEM,\lambda_2}(r)}$	$\frac{r}{e_{min}}$	$\sigma^E_{FEM,\lambda_2}(r)$ [MPa]	$\frac{\sigma^E_{FEM,\lambda_2}(r)}{\sigma^{E*}_{FEM,\lambda_2}(r)}$	$\frac{K^E_{\sigma,\lambda_2}}{K^{E*}_{\sigma,\lambda_2}}$
0.0	-0.010	0.873	0.00	-0.011	0.932	
0.5	-0.016	0.866	0.5	-0.016	0.908	
1.0	-0.016	0.868	1.0	-0.017	0.923	0.970
1.5	-0.016	0.875	1.5	-0.017	0.923	
2.0	-0.016	0.879	2.0	-0.016	0.926	

Table 4a
ISSFs at Point A, K^A_{σ,λ_1^A}, K^A_{σ,λ_2^A}, K^A_{τ,λ_1^A}, K^A_{τ,λ_2^A} in Fig. 1 for the material combination in Table 1(a).

l_{in} [μm]	K^A_{σ,λ_1^A} [MPa · m$^{1-0.7784}$]	K^A_{σ,λ_2^A} [MPa · m$^{1-0.6158}$]	K^A_{τ,λ_1^A} [MPa · m$^{1-0.7784}$]	K^A_{τ,λ_2^A} [MPa · m$^{1-0.6158}$]
50	0.214	0.288	0.126	0.182
100	0.154	0.224	0.0907	0.141
150	0.126	0.185	0.0742	0.117
200	0.109	0.163	0.0642	0.103
250	0.0970	0.147	0.0572	0.0929
300	0.0875	0.134	0.0516	0.0846
350	0.0805	0.124	0.0475	0.0785
400	0.0749	0.116	0.0441	0.0733
450	0.0698	0.109	0.0411	0.0687
500	0.0658	0.103	0.0388	0.0650
1000	0.0430	0.0689	0.0253	0.0435

Table 4b
ISSFs at point A, K^A_{σ,λ_1^A}, K^A_{σ,λ_2^A}, K^A_{τ,λ_1^A}, K^A_{τ,λ_2^A} in Fig. 1 for the material combination in Table 1 (b).

l_{in} [μm]	K^A_{σ,λ_1^A} [MPa · m$^{1-0.7632}$]	K^A_{σ,λ_2^A} [MPa · m$^{1-0.6218}$]	K^A_{τ,λ_1^A} [MPa · m$^{1-0.7632}$]	K^A_{τ,λ_2^A} [MPa · m$^{1-0.6218}$]
50	0.220	0.343	0.128	0.175
100	0.152	0.258	0.0885	0.131
150	0.120	0.207	0.0696	0.106
200	0.101	0.177	0.0585	0.0905
250	0.0873	0.156	0.0507	0.0796
300	0.0767	0.139	0.0445	0.0706
350	0.0689	0.126	0.0400	0.0641
400	0.0627	0.115	0.0364	0.0587
450	0.0571	0.106	0.0332	0.0538
500	0.0528	0.0980	0.0307	0.0500
1000	0.0296	0.0565	0.0172	0.0288

Table 5a
ISSFs at point E, K^E_{σ,λ_1^E}, K^E_{σ,τ_1^E} in Fig. 1 for the material combination in Table 1(a).

l_{in} [μm]	K^E_{σ,λ_1^E} [MPa · m$^{1-0.6752}$]	K^E_{τ,λ_1^E} [MPa · m$^{1-0.6752}$]
50	0.470	0.166
100	0.346	0.122
150	0.291	0.103
200	0.259	0.0915
250	0.238	0.0840
300	0.223	0.0787
350	0.212	0.0747
400	0.203	0.0717
450	0.196	0.0693
500	0.191	0.0674
1000	0.170	0.0599

Table 5b
ISSFs at point E, K^E_{σ,λ_1^E}, K^E_{σ,τ_1^E} in Fig. 1 for the material combination in Table 1(b).

l_{in} [μm]	K^E_{σ,λ_1^E} [MPa · m$^{1-0.6591}$]	K^E_{τ,λ_1^E} [MPa · m$^{1-0.6591}$]
50	0.530	0.197
100	0.433	0.161
150	0.389	0.144
200	0.364	0.135
250	0.349	0.130
300	0.339	0.126
350	0.332	0.123
400	0.326	0.121
450	0.322	0.120
500	0.319	0.119
1000	0.312	0.116

properties for the fiber and matrix are set to be same for the reference model and pull-out model, respectively. In other words, material properties of fiber in Fig. 2(b) and inclusion in Fig. 2(b) are set to be the same.

FEM stress distributions along the interfaces near Point A of different mesh size are shown in Tables 2a and b. Results of inclusion model when $l_{in} = 500\mu$m and pull-out model when $l_{in} = 100\mu$m are shown as example. As shown in Table 2a $\sigma^A_{1,FEM}(r)$ is FEM stress distribution,

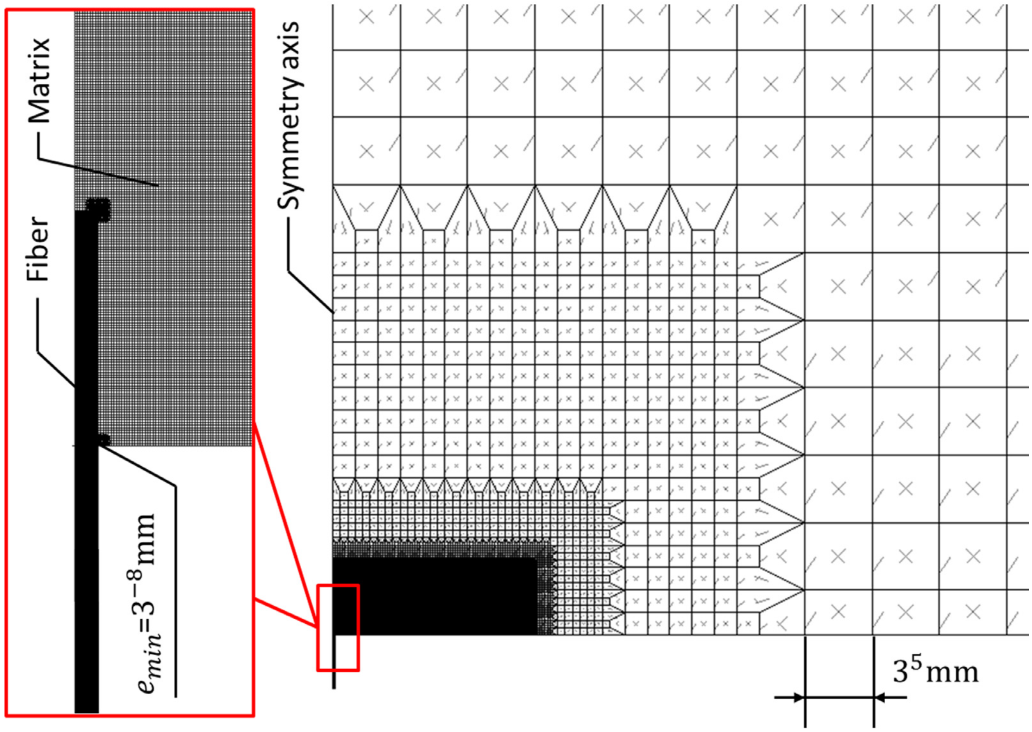

Fig. 3. FEM mesh pattern.

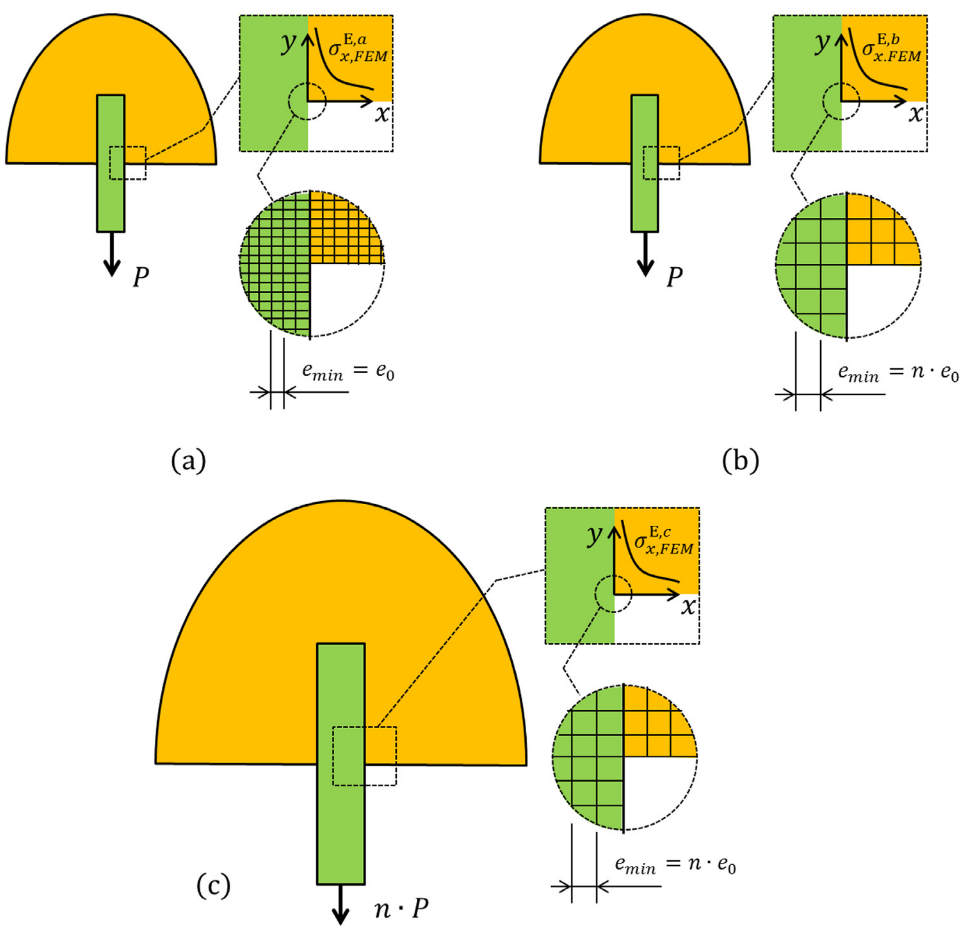

Fig. 4. Schematic illustration of Point E FEM models.

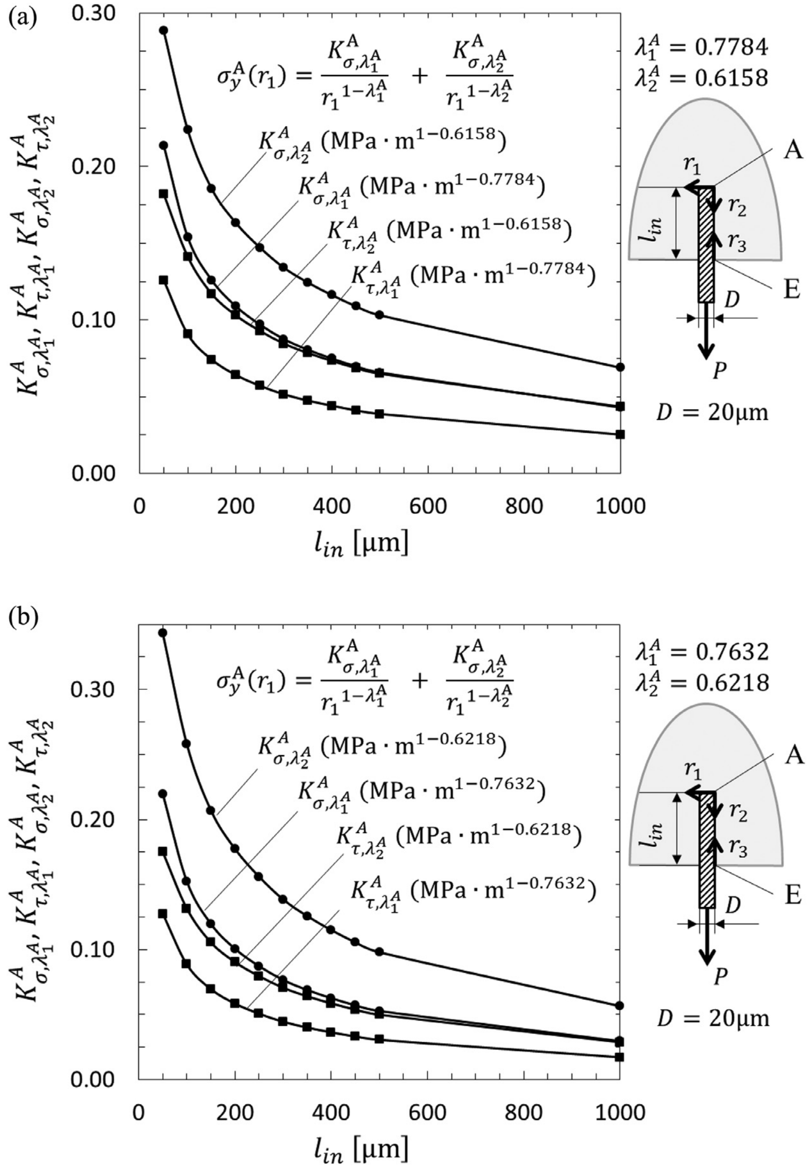

Fig. 5. (a). ISSFs at Point A vs. embedding length for Carbon Fiber/Epoxy. (b). ISSFs at Point A vs. embedding length for Glass Fiber/Epoxy.

corresponding to λ_1^A, of carbon fiber/epoxy as shown in Table 1a, when $l_{in} = 100\mu$m in pull-out model. $\sigma^{A*}_{I,\ FEM}(r)$ is FEM stress distribution, corresponding to λ_1^A, of the same material combination, when $l_{in} = 500\mu m$ in the reference model, whose ISSF can be calculated by BFM. Similarly, $\sigma^A_{II,\ FEM}(r)$ in the pull-out model and $\sigma^{A*}_{II,\ FEM}(r)$ in the reference model, corresponding to λ_2^A are shown in Table 2b. In addition, the FEM stress ratios $\sigma^A_{I,\ FEM}(r)/\sigma^{A*}_{I,\ FEM}(r)$, $\sigma^A_{II,\ FEM}(r)/\sigma^{A*}_{II,\ FEM}(r)$ are calculated from the above mentioned FEM stress distributions.

As shown in Tables 2a and b, the stress distributions $\sigma^A_{I,\ FEM}(r)$, $\sigma^A_{II,\ FEM}(r)$ are different depending on the mesh size. However, the stress ratio between unknown model and reference model, i.e. $\sigma^A_{I,\ FEM}(r)/\sigma^{A*}_{I,\ FEM}(r)$ and $\sigma^A_{II,\ FEM}(r)/\sigma^{A*}_{II,\ FEM}(r)$ are independent of mesh size, and keep in converges within four significant digits. In fact, the stress at the edge of the interface is infinite. Therefore, the value of the stress varies greatly depending on the mesh size. From the data shown in Tables 2a and b, it is found that the stress ratio between the pull-out problem and the reference problem can be obtained accurately independent of the mesh size. Then the ISSF of pull-out problem can be obtained from the FEM stress ratio and the ISSF of reference problems, as shown in Eq. (7).

3. Singular stress field and the ISSF at the fiber entry point

The singular stress field at Point E as shown in Fig. 2(a) is different from that of Point A but similar to the interface end for lap joints [33,64]. The value of singular indexes (λ_1^E, λ_2^E) around the corner E can be determined by solving the characteristic Eq. (8) [65,66]. For most of the material combinations the singular indexes λ_i^E have two real roots λ_1^E and λ_2^E corresponding to two different singular fields [67].

$$\begin{aligned} &4sin^2(\pi\lambda)\left\{sin^2\left(\frac{\pi\lambda}{2}\right) - \lambda^2\right\}\beta^2 + 4\lambda^2 sin^2(\pi\lambda)\alpha\beta \\ &+ \left\{sin^2\left(\frac{\pi\lambda}{2}\right) - \lambda^2\right\}\alpha^2 + 4\lambda^2 sin^2(\pi\lambda)\beta \\ &+ 2\left\{\lambda^2\cos(2\pi\lambda) + sin^2\left(\frac{\pi\lambda}{2}\right)\cos(\pi\lambda) + \frac{1}{2}sin^2(\pi\lambda)\right\}\alpha \\ &+ sin^2\left(\frac{3\pi\lambda}{2}\right) - \lambda^2 = 0 \end{aligned} \tag{8}$$

Here, α and β are defined by equation (A.1). Table 1 (a) shows for the Carbon/Epoxy material combination, $\alpha = 0.9775$, $\beta = 0.2250$, $\lambda_1^E = 0.6751$, $\lambda_2^E = 0.9999$. Note that the singular index $\lambda_2^E = 0.9999$ for K^E_{σ,λ_2^E} is very close to 1, corresponding to almost no singularity having little effect on the singular stress distribution.

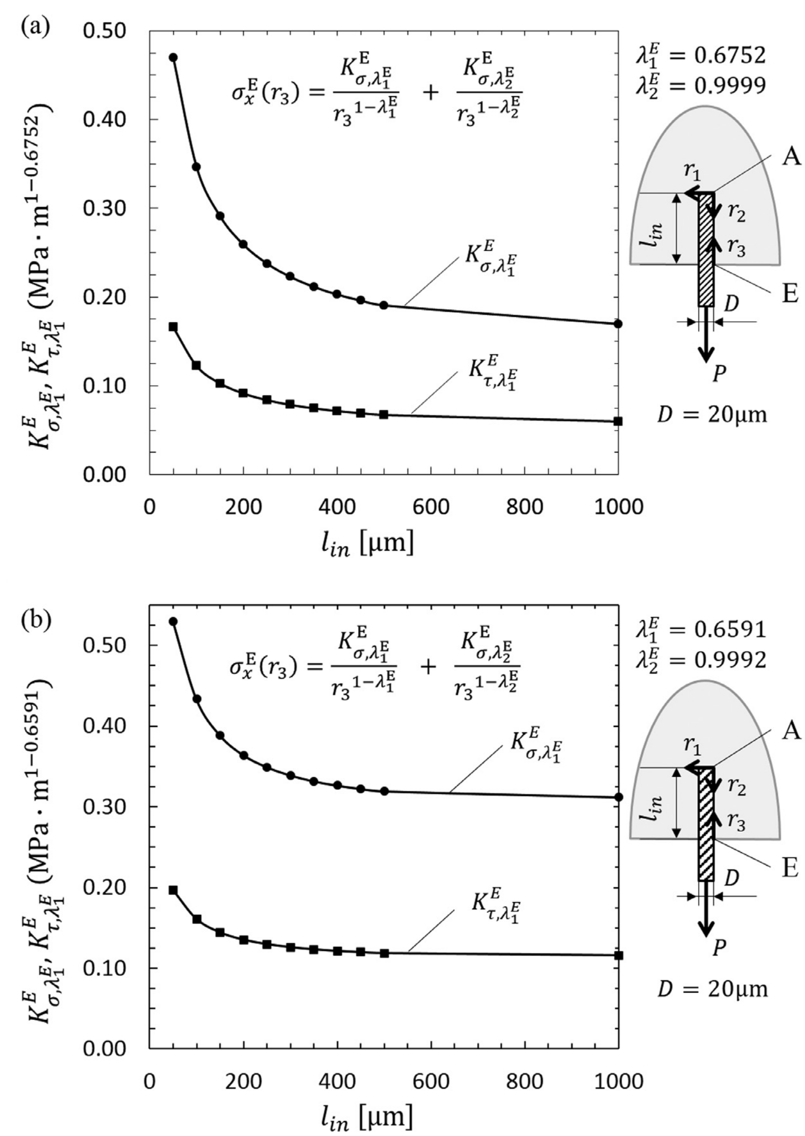

Fig. 6. (a). ISSFs at Point E vs. embedding length for Carbon Fiber/Epoxy. (b). ISSFs at Point E vs. embedding length for Glass Fiber/Epoxy.

The singular stress field at the vicinity of Point E in Fig. 1 can be expressed as Eq. (9). This singular stress field is identical to that of lap joints [33,64].

$$\begin{cases} \sigma_x^{\mathrm{E}}(r_3) = \dfrac{K^{\mathrm{E}}_{\sigma,\,\lambda_1^{\mathrm{E}}}}{r_3^{\,1-\lambda_1^{\mathrm{E}}}} + \dfrac{K^{\mathrm{E}}_{\sigma,\,\lambda_2^{\mathrm{E}}}}{r_3^{\,1-\lambda_2^{\mathrm{E}}}} \\ \tau_{xy}^{\mathrm{E}}(r_3) = \dfrac{K^{\mathrm{E}}_{\tau,\,\lambda_1^{\mathrm{E}}}}{r_3^{\,1-\lambda_1^{\mathrm{E}}}} + \dfrac{K^{\mathrm{E}}_{\tau,\,\lambda_2^{\mathrm{E}}}}{r_3^{\,1-\lambda_2^{\mathrm{E}}}} \end{cases} \tag{9}$$

As the reference solution Reciprocal work contour integral method (RWCIM) can be used [33,34,64,68]. Recently, Miyazaki et al. [34,35] proposed a technique of how to obtain two ISSFs corresponding to two distinct singular stress fields by applying proportional method. To apply this method to the pull-out problem, Fig. 4 illustrates 3 kinds of the pull-out models used in this technique.

The model (a) has minimum elements whose size $e_{min} = e_0$. The FEM stress of the model (a) is denoted by $\sigma^{E,a}_{x,FEM}(r_3)|_{e_{min}=e_0}$ and the ISSFs in model (a) are denoted by $K^{E,a}_{\sigma,\lambda_1^E}$ and $K^{E,a}_{\sigma,\lambda_2^E}$. Here, r_3 is the distance from the corner edge Point E in Fig. 2(a). The model (b) has the same size of the model (a) but having larger minimum elements $e_{min} = n \cdot e_0$ compared to model (a). The FEM stress of model (b) is denoted by $\sigma^{E,b}_{x,FEM}(r_3)|_{e_{min}=n\cdot e_0}$ and the ISSFs in model (b) are denoted by $K^{E,b}_{\sigma,\lambda_1^E}$ and $K^{E,b}_{\sigma,\lambda_2^E}$. The model (c) is n times larger than models (a) including all elements and therefore having the same minimum mesh size of model (b). The FEM stress of model (c) is denoted by $\sigma^{E,c}_{x,FEM}(r_3)|_{e_{min}=n\cdot e_0}$. It can be verified that the stress $\sigma^{E,c}_{x,FEM}$ at $n \cdot r_0$ is equal to the stress $\sigma^{E,a}_{x,FEM}$ at r_0. The ISSFs in model (c) are denoted by $K^{E,c}_{\sigma,\lambda_1^E}$ and $K^{E,c}_{\sigma,\lambda_2^E}$. The FEM stress $\sigma^{E,a}_{x,FEM}$ should be divided into $\sigma^{E,a}_{x,FEM,\lambda_1}$ and $\sigma^{E,a}_{x,FEM,\lambda_2}$ to calculate two ISSFs K^E_{σ,λ_1} and K^E_{σ,λ_2}.

$$\sigma^{E,a}_{x,FEM} = \sigma^{E,a}_{FEM,\lambda_1} + \sigma^{E,a}_{FEM,\lambda_2} \tag{10}$$

Similarly, $\sigma^{E,b}_{x,FEM}$ and $\sigma^{E,c}_{x,FEM}$ should be divided.

$$\sigma^{E,b}_{x,FEM} = \sigma^{E,b}_{FEM,\lambda_1} + \sigma^{E,b}_{FEM,\lambda_2} \tag{11a}$$

$$\sigma^{E,c}_{x,FEM} = \sigma^{E,c}_{FEM,\lambda_1} + \sigma^{E,c}_{FEM,\lambda_2} \tag{11b}$$

The stress distribution $\sigma^{E,c}_{x,FEM}(r_3)$ at $r_3 = n \cdot r_0$ is exactly equal to the stress $\sigma^{E,a}_{x,FEM}(r_3)$ at $r_3 = r_0$ as shown in Eq. (12).

$$\frac{K^{E,a}_{\sigma,\lambda_1^E}}{(r_0)^{1-\lambda_1^E}} + \frac{K^{E,a}_{\sigma,\lambda_2^E}}{(r_0)^{1-\lambda_2^E}} = \frac{K^{E,c}_{\sigma,\lambda_1^E}}{(n\cdot r_0)^{1-\lambda_1^E}} + \frac{K^{E,c}_{\sigma,\lambda_2^E}}{(n\cdot r_0)^{1-\lambda_2^E}} \tag{12}$$

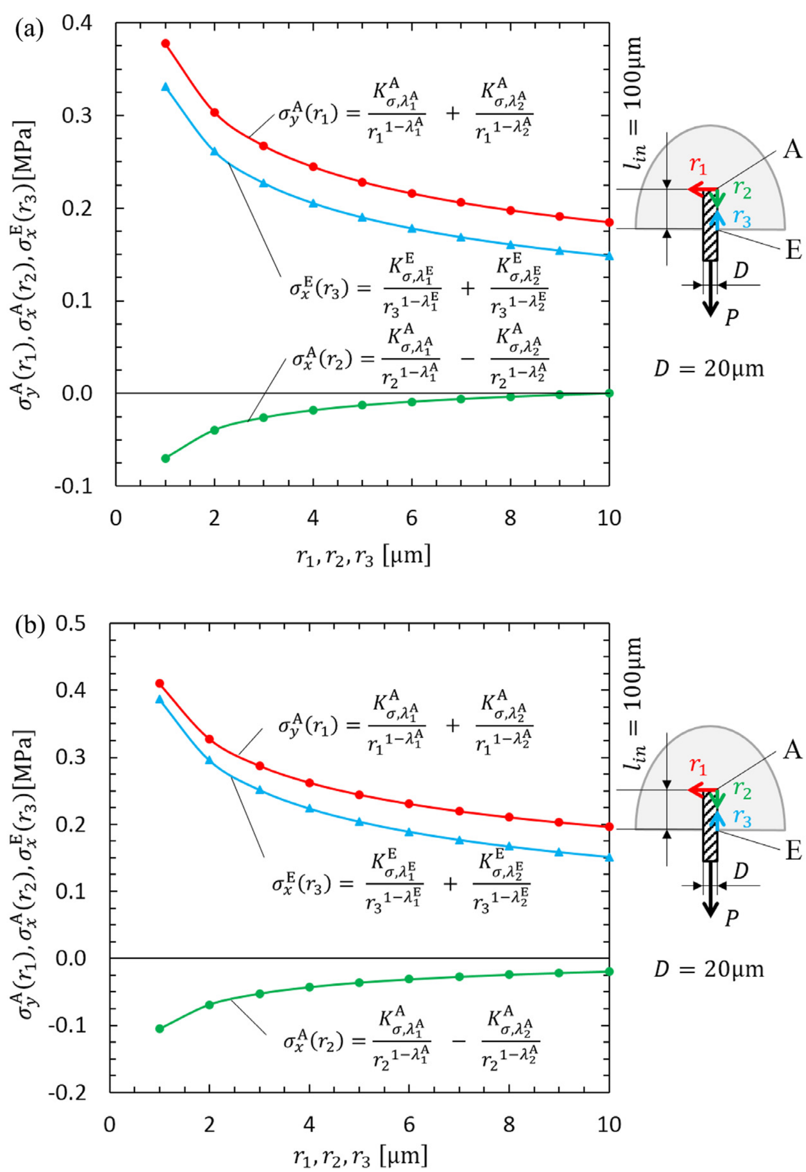

Fig. 7. (a). Stress distributions when $l_{in} = 100\ \mu$m for Carbon Fiber/Epoxy in Table 1. (b). Stress distributions when $l_{in} = 100\ \mu$m for Glass Fiber/Epoxy in Table 1.

From Eq. (12) the following relation between $K^{E,a}_{\sigma,\lambda_1^E}$ and $K^{E,c}_{\sigma,\lambda_1^E}$ can be derived.

$$\begin{cases} \dfrac{K^{E,c}_{\sigma,\lambda_1^E}}{K^{E,a}_{\sigma,\lambda_1^E}} = n^{1-\lambda_1^E} \\ \dfrac{K^{E,c}_{\sigma,\lambda_2^E}}{K^{E,a}_{\sigma,\lambda_2^E}} = n^{1-\lambda_2^E} \end{cases} \tag{13}$$

Since the mesh pattern is the same at the vicinity of Point E in model (b) and model (c), the following relation can be verified.

$$\begin{cases} \dfrac{K^{E,c}_{\sigma,\lambda_1^E}}{K^{E,b}_{\sigma,\lambda_1^E}} = \dfrac{\sigma^{E,c}_{FEM,\ \lambda_1}(n \cdot r_0)}{\sigma^{E,b}_{FEM,\lambda_1}(n \cdot r_0)} \\ \dfrac{K^{E,c}_{\sigma,\lambda_2^E}}{K^{E,b}_{\sigma,\lambda_2^E}} = \dfrac{\sigma^{E,c}_{FEM,\ \lambda_2}(n \cdot r_0)}{\sigma^{E,b}_{FEM,\lambda_2}(n \cdot r_0)} \end{cases} \tag{14}$$

Substituting Eq. (13) into Eq. (14) and using the $\sigma^{E,a}_{x,FEM}(r_3)|_{r_3=r_0} = \sigma^{E,c}_{x,FEM}(r_3)|_{r_3=n\cdot r_0}$, the following equation is obtained.

$$\begin{cases} \sigma^{E,b}_{FEM,\lambda_1}(n \cdot r_0) = \dfrac{\sigma^{E,a}_{FEM,\lambda_1}(r_0)}{n^{1-\lambda_1^E}} \\ \sigma^{E,b}_{FEM,\lambda_2}(n \cdot r_0) = \dfrac{\sigma^{E,a}_{FEM,\lambda_2}(r_0)}{n^{1-\lambda_2^E}} \end{cases} \tag{15}$$

Substituting Eq. (15) into Eq. (11a) the following equation is obtained [34,35].

$$\begin{aligned} \sigma^{E,b}_{x,FEM} &= \sigma^{E,b}_{FEM,\lambda_1} + \sigma^{E,b}_{FEM,\lambda_2} \\ &= \frac{\sigma^{E,a}_{FEM,\lambda_1}}{n^{1-\lambda_1^E}} + \frac{\sigma^{E,a}_{FEM,\lambda_2}}{n^{1-\lambda_1^E}} \end{aligned} \tag{16}$$

When the simultaneous Eqs. (10) and (16) are solved on the $\sigma^{E,a}_{x,FEM,\lambda_1}$ and $\sigma^{E,a}_{x,FEM,\lambda_2}$, the following equations are obtained. By using this method, the stress distributions corresponding to the two indexes

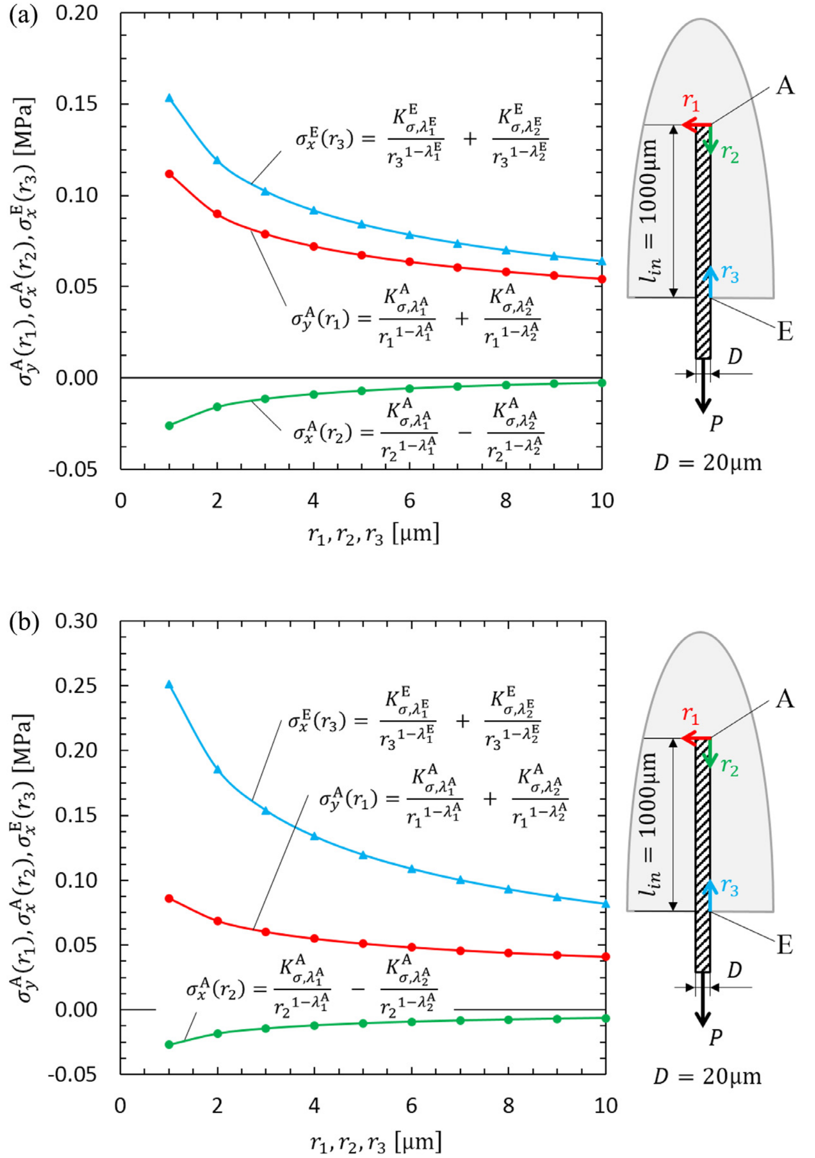

Fig. 8. (a). Stress distributions when $l_{in} = 1000$ μm for Carbon Fiber/Epoxy in Table 1. (b). Stress distributions when $l_{in} = 1000$ μm for Glass Fiber/Epoxy in Table 1.

λ_1^E, λ_2^E can be obtained in FEM.

$$\begin{cases} \sigma^{E,a}_{FEM,\lambda_1} = \dfrac{\sigma^{E,a}_{x,FEM}}{1-n^{\lambda_1-\lambda_2}} - \dfrac{\sigma^{E,b}_{x,FEM}}{n^{\lambda_2-1}-n^{\lambda_1-1}} \\ \sigma^{E,a}_{FEM,\lambda_2} = \dfrac{\sigma^{E,a}_{x,FEM}}{1-n^{\lambda_2-\lambda_1}} + \dfrac{\sigma^{E,b}_{x,FEM}}{n^{\lambda_2-1}-n^{\lambda_1-1}} \end{cases} \tag{17}$$

As shown in Eq. (18), if the ISSFs $K^{E^*}_{\sigma,\lambda_1}$ and $K^{E^*}_{\sigma,\lambda_2}$ are known in a reference problem, the ISSFs of a unknown problem can be obtained from FEM stress ratio $\sigma^{E}_{FEM,\lambda_1}(r)/\sigma^{E^*}_{FEM,\lambda_1}(r)$ and $\sigma^{E}_{FEM,\lambda_2}(r)/\sigma^{E^*}_{FEM,\lambda_2}(r)$. Here, $\sigma^{E}_{FEM,\lambda_1}(r)$ and $\sigma^{E}_{FEM,\lambda_2}(r)$ are FEM stress distributions in the model corresponding to unknown problem, and are divided by using Eq. (17). Similarly, $\sigma^{E^*}_{FEM,\lambda_1}(r)$ and $\sigma^{E^*}_{FEM,\lambda_2}(r)$ corresponding to the reference problem.

$$\begin{cases} \dfrac{K^{E}_{\sigma,\lambda_1}}{K^{E^*}_{\sigma,\lambda_1}} = \dfrac{\sigma^{E}_{FEM,\lambda_1}}{\sigma^{E^*}_{FEM,\lambda_1}} \\ \dfrac{K^{E}_{\sigma,\lambda_2}}{K^{E^*}_{\sigma,\lambda_2}} = \dfrac{\sigma^{E}_{FEM,\lambda_2}}{\sigma^{E^*}_{FEM,\lambda_2}} \end{cases} \tag{18}$$

Tables 3a and b shows FEM stress ratio $\sigma^{E}_{FEM,\lambda_1}(r)/\sigma^{E^*}_{FEM,\lambda_1}(r)$ and $\sigma^{E}_{FEM,\lambda_2}(r)/\sigma^{E^*}_{FEM,\lambda_2}(r)$ for Carbon Fiber/Epoxy in Table 1(a) obtained by using the technique described above. Here, $\sigma^{E}_{FEM,\lambda_1}(r)$ is the value for $l_{in} = 100$μm and $\sigma^{E^*}_{FEM,\lambda_2}(r)$ is the value for $l_{in} = 200$μm. In Table 3a, the stress ratio is independent of the mesh size and coincides with the results of RWCIM, which is explained in the Appendix C. In Table 3b, however, the stress ratio varies by about 10% error. This is because the singular index $\lambda_2^E = 0.9999 \approx 1$. Since $\lambda_2^E \approx 1$ means almost no singularity with smaller values $K^E_{\sigma,\lambda_2^E}/r_3^{1-\lambda_2^E}$ and $K^E_{\tau,\lambda_2^E}/r_3^{1-\lambda_2^E}$ in Eq. (9), the singular stress is mainly controlled only by K^E_{σ,λ_1^E} and K^E_{τ,λ_1^E} [28,29]. The RWCIM can be used to obtain the reference values although a large calculation time is necessary for the integral path. The proportional method can be conveniently focusing on the singular point to calculate the ISSFs by varying the fiber dimensions.

4. Results and discussion

In short fiber reinforced composites most fibers' aspect ratios are close to $l/D = 30$ [38]. In this study, assume the fiber width $D = 20$ μm and the total fiber length $l = 600$ μm. If half of the fiber length is embedded in the matrix, as shown in Fig. 2(a), the fiber embedded length is about $l_{in} = 300$ μm.

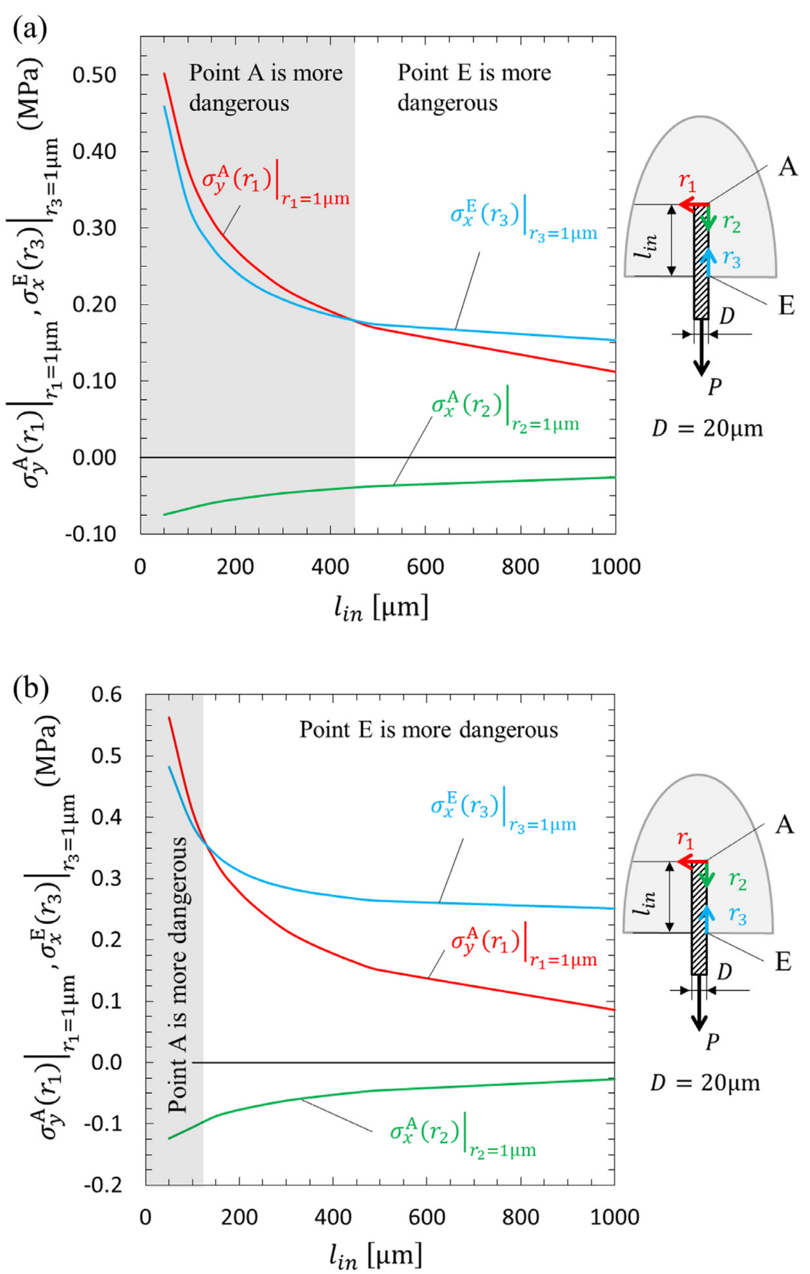

Fig. 9. (a). Stress at $r = 1\,\mu$m of different embedding length for Carbon Fiber/Epoxy. (b). Stress at $r = 1\,\mu$m of different embedding length for Glass Fiber/Epoxy

4.1. ISSF at point A

Table 4a and Fig. 5a show the ISSFs denoted by $K^{A}_{\sigma,\lambda_1^A}$, $K^{A}_{\sigma,\lambda_2^A}$, K^{A}_{τ,λ_1^A}, K^{A}_{τ,λ_2^A} [5] at Point A for carbon fiber/epoxy by varying l_{in} varies from 50 μm to 1000 μm. Table 4b and Fig. 5(b) show the ISSFs for glass fiber/epoxy. It is seen that ISSFs decrease with increasing l_{in}. This is consistent with the experimental results showing that the maximum pull-out force increases with increasing l_{in} [8,69].

By assuming the total fiber length of $l = 600\,\mu m$, the ISSFs are compared when $l_{in} = 150\,\mu m$ (1/4 embedded length) and $l_{in} = 300\,\mu m$ (1/2 embedded length). As shown in Table 4a for carbon fiber/epoxy, mode I ISSF, $K^{A}_{\sigma,\lambda_1^A}$ =0.0875 at $l_{in} = 300\,\mu m$ is 30.6% smaller than $K^{A}_{\sigma,\lambda_1^A}$ =0.126 at $l_{in} = 150\,\mu m$ and the modeIIISSF $K^{A}_{\sigma,\lambda_2^A}$ =0.134 at $l_{in} = 300\,\mu m$ is 27.6% smaller than $K^{A}_{\sigma,\lambda_2^A}$ =0.185 at $l_{in} = 150\,\mu m$.

As shown in Table 4b for glass fiber/epoxy, mode I ISSF $K^{A}_{\sigma,\lambda_1^A}$ =0.0767 at $l_{in} = 300\,\mu m$ is 36.1% smaller than $K^{A}_{\sigma,\lambda_1^A}$ =0.120 at $l_{in} = 150\,\mu m$. Regarding Mode IIISSF, $K^{A}_{\sigma,\lambda_2^A}$ =0.139 at $l_{in} = 300\,\mu m$ is 32.8% smaller than $K^{A}_{\sigma,\lambda_2^A}$ =0.207 at $l_{in} = 150\,\mu m$. As shown in Fig. 5(b) and Table 4b, the ISSFs K^{A}_{τ,λ_1^A} and K^{A}_{τ,λ_2^A} are also about 40% smaller than the ISSFs $K^{A}_{\sigma,\lambda_1^A}$ and $K^{A}_{\sigma,\lambda_2^A}$ for glass fiber/epoxy.

It is seen that ISSFs at $l_{in} = 300\,\mu m$ are smaller than the ISSFs at $l_{in} = 150\,\mu m$. As shown in Fig. 5(a) and Table 4a, the ISSFs K^{A}_{τ,λ_1^A} and K^{A}_{τ,λ_2^A} are about 40% smaller than the ISSFs $K^{A}_{\sigma,\lambda_1^A}$ and $K^{A}_{\sigma,\lambda_2^A}$ for carbon fiber/epoxy. In Section 4.3, therefore, the ISSFs $K^{A}_{\sigma,\lambda_1^A}$ and $K^{A}_{\sigma,\lambda_2^A}$ will be discussed.

4.2. ISSF at point E

Table 5a and Fig. 6(a) shows ISSFs $K^{E}_{\sigma,\lambda_1^E}$, $K^{E}_{\sigma,\lambda_2^E}$ at Point E for carbon fiber/epoxy by varying l_{in} from 50 μm to 1000 μm. Regarding the first term $K^{E}_{\sigma,\lambda_1^E}$ in Eq. (9) for carbon fiber/epoxy, $K^{E}_{\sigma,\lambda_1^E}$ = 0.223

at $l_{in} = 300$ μm is 23.4% smaller than $K^{E}_{\sigma,\lambda_1^E} = 0.291$ at $l_{in} = 150$ μm. Table 5b and Fig. 6(b) show the ISSFs for glass fiber/epoxy. The ISSF at Point E decreases with increasing l_{in}. Regarding the first term $K^{E}_{\sigma,\lambda_1^E}$ in Eq. (9) for glass fiber/epoxy, $K^{E}_{\sigma,\lambda_1^E} = 0.339$ at $l_{in} = 300$ μm is 12.9% smaller than $K^{E}_{\sigma,\lambda_1^E} = 0.389$ at $l_{in} = 150$ μm. The ISSF decreasing rate at Point E becomes smaller than that at Point A especially when $l_{in}$is large. Since the ISSF K^{E}_{τ,λ_1^E} is 60% smaller than the ISSF $K^{E}_{\sigma,\lambda_1^E}$ for this material combination, $K^{E}_{\sigma,\lambda_1^E}$ is discussed in the next section.

4.3. Comparison between Point A and Point E

When the single embedded fiber is under pull-out force, singular stress fields should be compared at Point A and Point E. However, those singular stress fields are different in properties, it is not possible to compare those two ISSFs directly. Therefore, the normal stress distributions along the interfaces between the fiber and matrix are focused. The shear-lag theory [15–17] has been widely used to discussed stress distribution, but is not enough for discussing the singular stress fields. This is because the shear-lag theory is based on a simple one-dimensional approximation of the fiber.

The comparison of stress distributions along the interfaces are shown in Figs. 7 and 8, that is, $\sigma_y^A(r_1)$ along r_1 , $\sigma_x^A(r_2)$ along r_2 around Point A in Fig. 1 and $\sigma_x^E(r_3)$ along r_3 around Point E. Equations used in Fig. 7 are Eqs. (1) and (2) [5] and (9) [6,7], as shown in Fig. 1. Since compressive stress $\sigma_x^A(r_2)$ does not cause the debonding directly, $\sigma_y^A(r_1)$ and $\sigma_x^E(r_3)$ are mainly compared in the following discussion. As shown in Fig. 7(a) for carbon fiber/epoxy and Fig. 7(b) for glass fiber/epoxy when $l_{in} = 100$ μm, since the stress $\sigma_y^A(r_1)$ at Point A is larger than the stress $\sigma_x^E(r_3)$ at Point E, debonding may occur at Point A earlier. On the other hand, when $l_{in} = 1000$ μm in Figs. 7(b) and 8(b), since the stress $\sigma_y^E(r_3)$ at point E is larger than the stress $\sigma_y^A(r_1)$ at point A, debonding may occur earlier at Point E.

Fig. 9 shows the comparison of stress $\sigma_y^A(r_1)$ at $r_1 = 1\mu$m close to Point A and the stress $\sigma_x^E(r_3)$ at $r_3 = 1\mu$m close to Point E by varying l_{in}.The fixed position $r_1 = r_3 = 1\mu$m is selected because the singular stress having different singular indexes. In Fig. 9(a) when $l_{in} = 450\mu$m, the severity at Point A and Point E is almost the same for carbon fiber/epoxy based on the assumption $\sigma_y^A(r_1)|_{r_1=1\mu m} = \sigma_x^E(r_3)|_{r_3=1\mu m}$. If the stress at different position $r_1 = r_3 \neq 1\mu$m is used, for example, if the stresses at $r_1 = r_3 = 2\mu$m are compared, the severities are almost the same when $l_{in} = 425\mu$m at Point A and Point E. As shown in Fig. 9(b), when $l_{in} = 150\mu$m, the severities of Point A and Point E are almost the same for glass fiber/epoxy.

5. Conclusions

In this paper, a partially-embedded single-fiber under pull-out force was considered focusing on two distinct singular stress fields appearing at fiber end and entry points. To compare the severities, singular stress distributions were obtained analytically along the interfaces along the fiber end and along the fiber entry interface. Then, the following conclusions were obtained.

(1) The mixed-mode ISSFs at the fiber end denoted by $K^{A}_{\sigma,\lambda_1^A}$, $K^{A}_{\sigma,\lambda_2^A}$ decrease with increasing the fiber embedded length l_{in}. Under fixed fiber length $l = 600$ μm, the ISSFs at $l_{in} = (1/2)l$ is about 30% smaller than the ISSFs at $l_{in} = (1/4)l$ for carbon fiber/epoxy, and the ISSFs at $l_{in} = (1/2)l$ is about 40% smaller than the ISSFs at $l_{in} = (1/4)l$ for glass fiber/epoxy.
(2) The two ISSFs denoted by $K^{E}_{\sigma,\lambda_1^E}$, $K^{E}_{\sigma,\lambda_2^E}$ at the fiber entry point decrease with increasing the fiber embedded length l_{in}. For example, the ISSFs at $l_{in} = (1/2)l$ is about 20% smaller than at $l_{in} = (1/4)l$ for carbon fiber/epoxy. The ISSFs at $l_{in} = (1/2)l$ is about 10% smaller than the ISSFs at $l_{in} = (1/4)l$ for glass fiber/epoxy. The ISSF decreasing rate at Point E becomes smaller than that at Point A especially when l_{in} is large.
(3) The severities were compared at the fiber end and fiber entry point by focusing on the stress jut 1μm away from the singular point by varying l_{in} (see Fig. 9). For carbon fiber/epoxy, the severities at the fiber end and fiber entry point are almost the same when $l_{in} = 450\mu$m. For glass fiber/epoxy, the severities are almost the same when $l_{in} = 125\mu$m. For shorter embedded length, the buried fiber end becomes more dangerous.

Declaration of Competing Interest

The author(s) declare having no potential conflicts of interest with respect to the research, authorship, and/or publication of this article.

Acknowledgements

The authors wish to express our thanks to Professor Tatsujiro MIYAZAKI from University of the Ryukyus for his helpful advice on various technical issues discussed in this paper. The authors are thankful to the members of our research group, Mr Rei TAKAKI, Mr Biao WANG, and Ms Akane INOUE for their generous support for this study. The authors are grateful for the financial support provided by Japanese Government (Monbukagakusho: Mext).The authors, however, bears full responsibility for the paper.

Appendix A. ISSFs under Arbitrary Material Combination for a Single Rectangle Fiber in an Infinite Plate Subjected to Remote Tension

In this Appendix, the intensity of singular stress fields (ISSFs) in Fig. 2(b) are shown in the $\alpha-\beta$ space. Here, α, β denote Dundurs bi-material parameters [41], which are defined by equation (A.1). Here, G_F and G_M are shear modulus, which can be transformed from Young's modulus E_F, E_M and Poisson's Ratios ν_F, ν_M. Subscripts M, F represent the matrix and reinforcing fiber, respectively. In this study, analysis is carried out on the basis of plane assumption.

$$\begin{cases} \alpha = \dfrac{G_F(\kappa_M+1)-G_M(\kappa_F+1)}{G_F(\kappa_M+1)+G_M(\kappa_F+1)} \\ \beta = \dfrac{G_F(\kappa_M-1)-G_M(\kappa_F-1)}{G_F(\kappa_M+1)+G_M(\kappa_F+1)} \end{cases}, \kappa_i = \begin{cases} (3-\nu_i)/(1+\nu_i)\ (Plain\ stress) \\ (3-4\nu_i)\ (Plain\ strain) \end{cases} (i = M, F). \tag{A.1}$$

By using the BFM coupled with singular integral equation [36,37,42], the following ISSFs F_I^* and F_{II}^* at Point A* in Fig. 2(b) can be calculated. Here, the fiber's total length is fixed as the aspect ratio $l/D = 10$. For the material combination (a) in Table 1, the convergency of the solution is shown in Table A.1 by varying the number of collocation M increasing the order of polynomial approximation at each boundary division. Four digits accuracy can be seen. The normalized ISSFs in Fig. 2(b) defined by Eq. (5) are shown in Table A.2.a, A.2.b and Fig. A.1 under arbitrary material combination.

Singular indexes λ_1^A and λ_2^A around the corner A and corner A*can be calculated by solving equations (A.2a) and (A.2b) on λ, respectively [36,42].

Table A.1
Convergence of the ISSFs in Fig. 2(b) for the material combination in Table 1(a).

M	$F_I^* = K^*_{I,\lambda_1^A}/[\sigma_\infty\sqrt{\pi}(D/2)^{1-\lambda_1^A}]$	$F_{II}^* = K^*_{II,\lambda_2^A}/[\sigma_\infty\sqrt{\pi}(D/2)^{1-\lambda_2^A}]$
8	0.6780	1.132
7	0.6782	1.133
6	0.6780	1.133
5	0.6783	1.130

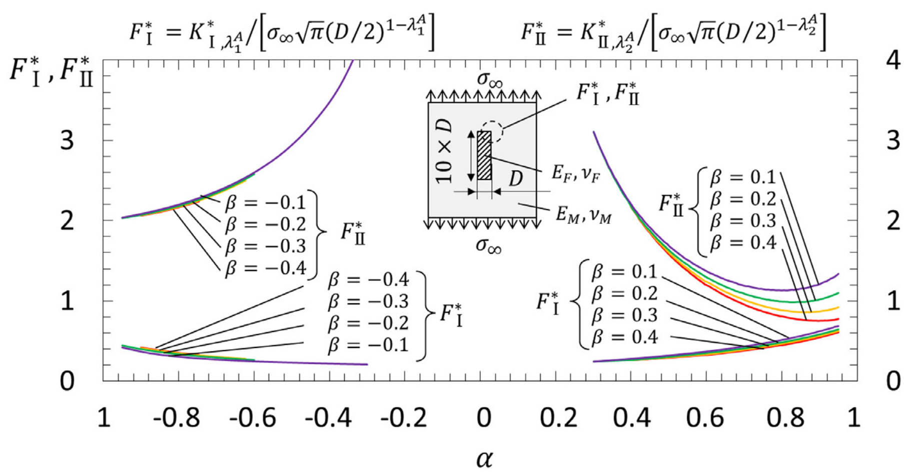

Fig. A.1. ISSFs for a single rectangle fiber in an infinite plate subjected to remote tension in Fig. 2(b).

Table A.2.a
F^*_{I} for a Single Rectangle Fiber in an Infinite Plate Subjected to Remote Tension in Fig. 2(b) when l/D = 10.

	$\alpha = 0.9$	0.8	0.7	0.6	0.5	0.4	0.3
$\beta = 0.1$	0.623	0.513	0.434	0.370	0.322	0.280	0.245
$\beta = 0.2$	0.584	0.484	0.412	0.353	0.304	0.265	–
$\beta = 0.3$	0.563	0.469	0.393	0.334	0.297	–	–
$\beta = 0.4$	0.547	0.449	0.382	–	–	–	–

Table A.2.b
F^*_{II} for a Single Rectangle Fiber in an Infinite Plate Subjected to Remote Tension in Fig. 2(b) when l/D = 10.

	$\alpha = 0.9$	0.8	0.7	0.6	0.5	0.4	0.3
$\beta = 0.1$	1.208	1.131	1.189	1.371	1.675	2.198	3.106
$\beta = 0.2$	1.019	0.993	1.086	1.290	1.629	2.141	–
$\beta = 0.3$	0.870	0.883	1.014	1.240	1.598	–	–
$\beta = 0.4$	0.753	0.810	0.955	–	–	–	–

Here, the singular indexes λ_1^A and λ_2^A have real values in the range $0 < Re(\lambda_i^A) < 1$ if $\beta(\alpha-\beta) > 0$. In equations (A.2), we can put $\gamma = \pi/2$ representing the angle between interfaces r_1 and r_2.

$$\begin{aligned} D_1(\alpha,\beta,\gamma,\lambda) &= (\alpha-\beta)^2\lambda^2[1-cos(2\gamma)] \\ &-2\lambda(\alpha-\beta)sin(\gamma)\{sin(\lambda\gamma)+sin[\lambda(2\pi-\gamma)]\} \\ &+2\lambda(\alpha-\beta)\beta\cdot sin(\gamma)\{sin[\lambda(2\pi-\gamma)]-sin(\lambda\gamma)\} \\ &+\left(1-\alpha^2\right)-\left(1-\beta^2\right)cos(2\lambda\pi) \\ &+\left(\alpha^2-\beta^2\right)\cos[2\lambda(\gamma-\pi)]=0 \end{aligned} \tag{A.2a}$$

$$\begin{aligned} D_2(\alpha,\beta,\gamma,\lambda) &= (\alpha-\beta)^2\lambda^2[1-cos(2\gamma)] \\ &+2\lambda(\alpha-\beta)sin(\gamma)\{sin(\lambda\gamma)+sin[\lambda(2\pi-\gamma)]\} \\ &-2\lambda(\alpha-\beta)\beta\cdot sin(\gamma)\{sin[\lambda(2\pi-\gamma)]-sin(\lambda\gamma)\} \\ &+\left(1-\alpha^2\right)-\left(1-\beta^2\right)cos(2\lambda\pi) \\ &+\left(\alpha^2-\beta^2\right)\cos[2\lambda(\gamma-\pi)]=0 \end{aligned} \tag{A.2b}$$

Appendix B. ISSFs under Arbitrary Material Combination for a Single Fiber Subjected to Pull-out Force from a Semi-Infinite Plate

In this Appendix, the ISSFs in Fig. 2(a) at the fiber buried end under pull-out are shown in the $\alpha-\beta$ space. The fiber embedding length is fixed as $l_{in}/D = 5$. Tables B.1.a, B.1.b and Fig. B.1 show the ISSF ratios for Fig. 2(a) and (b) obtained by using the proportional method explained in Section 2. Table B.2.a, B.2.b and Fig. B.2 show the normalized ISSFs at Point A in Fig. 2(a) calculated from the ISSF ratios and the ISSFs at Point A* shown in Appendix A.

Table B.1.a
$F_{\mathrm{I}}/F^*_{\mathrm{I}}$ when $l_{in}/D = 5$ in Fig. 2(a) and $l/D = 10$ in Fig. 2(b).

	$\alpha = 0.9$	0.8	0.7	0.6	0.5	0.4	0.3
$\beta = 0.1$	0.0864	0.111	0.128	0.139	0.145	0.146	0.143
$\beta = 0.2$	0.0862	0.108	0.122	0.130	0.133	0.132	–
$\beta = 0.3$	0.0851	0.105	0.116	0.122	0.123	–	–
$\beta = 0.4$	0.0832	0.100	0.110	–	–	–	–

Table B.1.b
$F_{\mathrm{II}}/F^*_{\mathrm{II}}$ when $l_{in}/D = 5$ in Fig. 2(a) and $l/D = 10$ in Fig. 2(b).

	$\alpha = 0.9$	0.8	0.7	0.6	0.5	0.4	0.3
$\beta = 0.1$	0.0766	0.0935	0.104	0.111	0.115	0.118	0.119
$\beta = 0.2$	0.0760	0.0928	0.103	0.109	0.113	0.115	–
$\beta = 0.3$	0.0749	0.0915	0.101	0.107	0.111	–	–
$\beta = 0.4$	0.0733	0.0895	0.0991	–	–	–	–

Table B.2.a
F_{I} when $l_{in}/D = 5$ in Fig. 2(a).

	$\alpha = 0.9$	0.8	0.7	0.6	0.5	0.4	0.3
$\beta = 0.1$	0.05384	0.05707	0.05569	0.05163	0.04673	0.04099	0.03502
$\beta = 0.2$	0.05032	0.05220	0.05019	0.04579	0.04052	0.03501	–
$\beta = 0.3$	0.04792	0.04898	0.04562	0.04065	0.03644	–	–
$\beta = 0.4$	0.04553	0.04511	0.04209	–	–	–	–

Table B.2.b
F_{II} when $l_{in}/D = 5$ in Fig. 2(a).

	$\alpha = 0.9$	0.8	0.7	0.6	0.5	0.4	0.3
$\beta = 0.1$	0.09249	0.10581	0.12418	0.15250	0.19326	0.25863	0.36925
$\beta = 0.2$	0.07743	0.09214	0.11202	0.14115	0.18444	0.24687	–
$\beta = 0.3$	0.06516	0.08079	0.10280	0.13304	0.17696	–	–
$\beta = 0.4$	0.05519	0.07249	0.09466	–	–	–	–

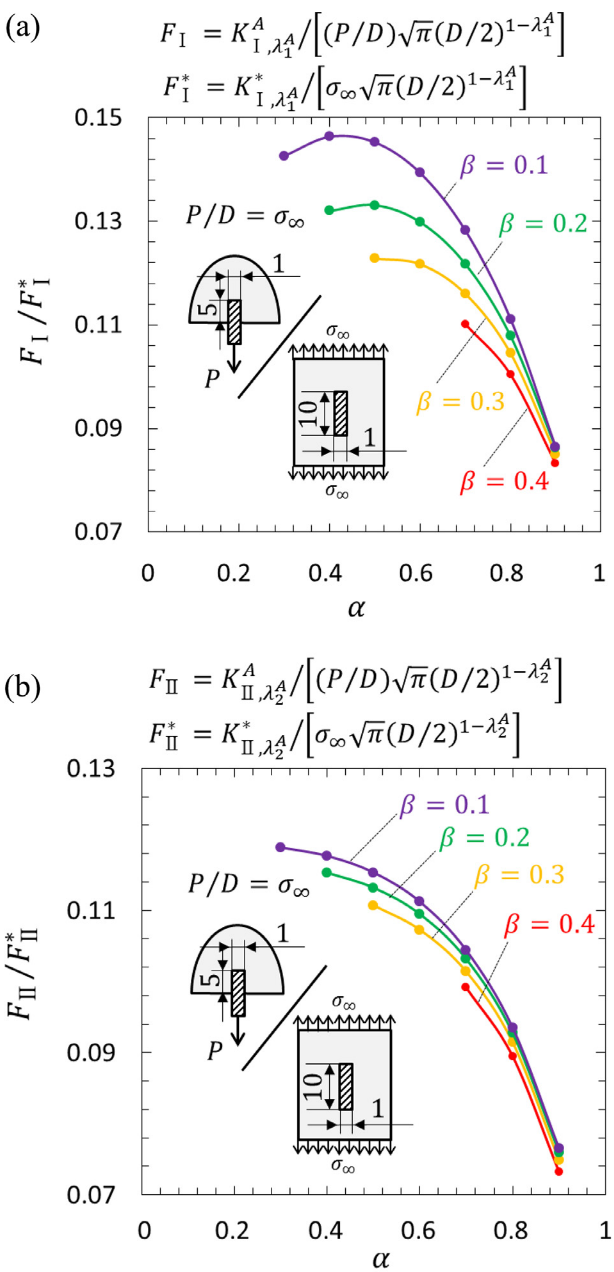

Fig. B.1. (a). FEM stress ratio. **B.1(b)** FEM stress ratio.

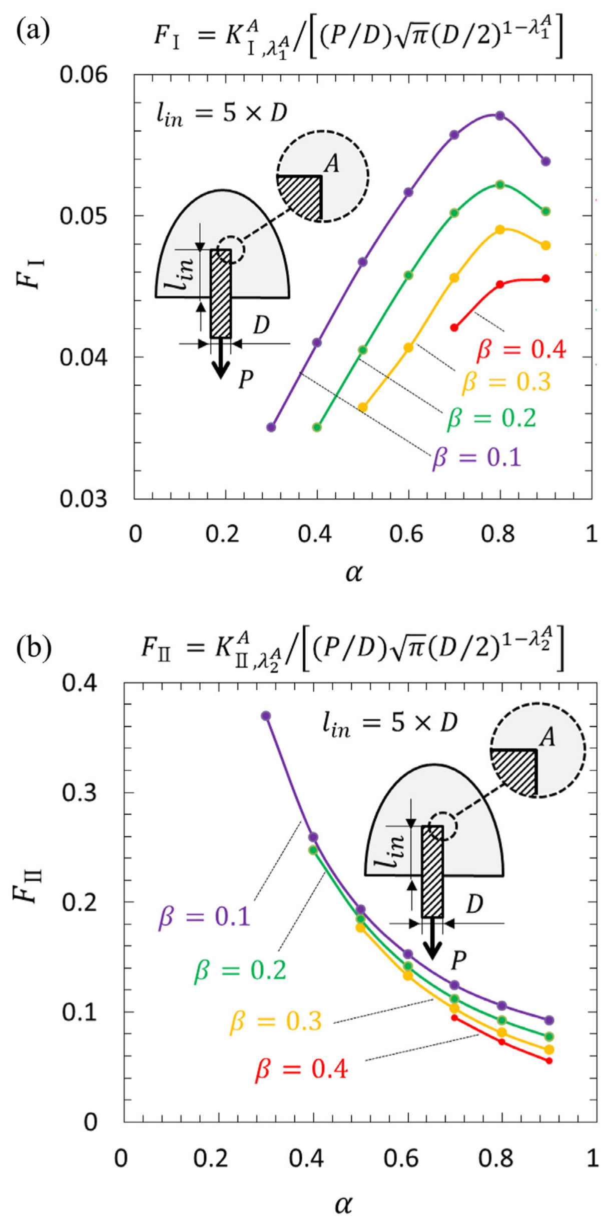

Fig. B.2. (a). F_{I} when $l_{in}/D = 5$ in Fig. 2(a). **B.2(b).** F_{II} when $l_{in}/D = 5$ in Fig. 2(a).

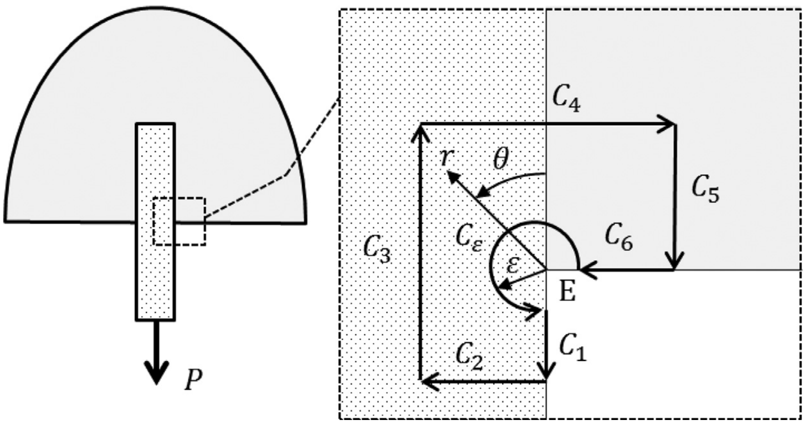

Fig. C.1. Integral path C for RWCIM ($C = C_1 + C_2 + C_3 + C_4 + C_5 + C_6$).

Appendix C. Reference Solution Obtained by Using Reciprocal Work Contour Integral Method (RWCIM)

The ISSFs $K^E_{\sigma,\,\lambda_1^E}$, $K^E_{\tau,\,\lambda_1^E}$ at the fiber entry Point E in Fig. 2(a) can be calculated by using the proportional method explained in Section 3 from the FEM stress ratios as shown in Eq. (18), which is $\frac{K^E_{\sigma,\lambda_1}}{K^{E*}_{\sigma,\lambda_1}} = \frac{\sigma^E_{FEM,\lambda_1}}{\sigma^{E*}_{FEM,\lambda_1}}$, $\frac{K^E_{\sigma,\lambda_2}}{K^{E*}_{\sigma,\lambda_2}} = \frac{\sigma^E_{FEM,\lambda_2}}{\sigma^{E*}_{FEM,\lambda_2}}$. To obtain the reference solution $K^{E*}_{\sigma,\,\lambda_1^E}$, $K^{E*}_{\tau,\,\lambda_1^E}$ The RWCIM may be suitable. This method is based on the concept of Betti's Law, pioneered by Stern et al. [46]. Carpenter et al. [68] and Sinclair et al. [70] adapted this method to the general opening crack problem. By mean of Williams′ eigenfunction expansion method, displacement and stress in the vicinity of the interface corner edge can be expressed as [68,71]:

$$\sigma_{ij} = \sum_{k=1}^{\infty} K_k f_{ij}(\theta, \lambda_k) r^{\lambda_k - 1} \tag{C.1}$$

$$u_i = \sum_{k=1}^{\infty} K_k g_i(\theta, \lambda_k) r^{\lambda_k} \tag{C.2}$$

Here, λ_k is singular index obtained by solving Eq. (8) in Section 3. For most of the material combinations the singular indexes λ_i^E have two real roots λ_1^E and λ_2^E corresponding to two different singular fields [67]. Here, K_k is ISSF corresponding to singular index λ_k, obtained by RWCIM discussed in this section. As shown in Fig. C.1, symbol r is the radial distance away from Point E. Eigenfunctions f_{ij} and g_i depend on λ_k and θ. When $\theta = 0$, and use $K_{\sigma,\,\lambda_k}$ to denote $K_k f_\theta(\theta, \lambda_k)$, equation (C.1) is expressed as Eq. (9). Denote by u_i the displacement field and σ_{ij} the traction vector on a contour $C = C_1 + C_2 + C_3 + C_4 + C_5 + C_6 + C_\varepsilon$, as shown in Fig. C.1, equation C.3 [68] is obtained from Betti's Law:

$$\oint_C \left(\sigma_{ij} u_i^* - \sigma_{ij}^* u_i\right) ds = 0. \tag{C.3}$$

Here, u_i^* and σ_{ij}^* correspond to any other such solution. Contour C_ε is a three-quarter circle contour with a radius ε. Separate the contour into C_ε and $C_R = C_1 + C_2 + C_3 + C_4 + C_5 + C_6$, equation C.3 becomes [72]:

$$I_\varepsilon = \int_{C_\varepsilon} \left(\sigma_{ij} u_i^* - \sigma_{ij}^* u_i\right) ds = -\int_{C_R} \left(\sigma_{ij} u_i^* - \sigma_{ij}^* u_i\right) ds. \tag{C.4}$$

Then, the integral I_ε can be calculated from the path independent contour C_R, without need for accurate data in the vicinity of the Point E in FEM calculation. ISSF K_k corresponding to singular index λ_k can then be obtained. Combined with f_{ij} for σ and τ respectively, expressed as $K^E_{\sigma,\,\lambda_1^E}$, $K^E_{\sigma,\,\lambda_2^E}$, $K^E_{\tau,\,\lambda_1^E}$, $K^E_{\tau,\,\lambda_2^E}$ in Section 3. Worth mentioning that, for the integral path C shown in Fig. C.1, contours C_1 and C_2 locate along the stress free surface, and therefore, the integrals along these contours are zero.

Plane strain condition is selected for carrying out the linear elastic analyses in MSC Marc software. Representation of the selected mesh pattern for developing these analyses is similar to that as shown in Fig. 3. Around the interface corner edge eight-node elements are utilized, while for other regions away from the interface corner edge, four-node elements are selected.

RWCIM can be used to provide the reference ISSFs. However, RWCIM requires a large number of calculations for complex operations with matrix as well as numerical integrations along the path. The proposed method in Section 3 to calculate the ISSFs (from a reference solution of the ISSF) is just as accurate as the RWCIM, when calculating the first term, being more convenient and practical. In this method, comparison between two models can be made from the FEM stress ratios, easily.

References

[1] Wu Q, Li M, Gu Y, Li Y, Zhang Z. Nano-analysis on the structure and chemical composition of the interphase region in carbon fiber composite. Compos Part A Appl Sci Manuf 2014;56:143–9. doi:10.1016/j.compositesa.2013.10.003.
[2] Teklal F, Djebbar A, Allaoui S, Hivet G, Joliff Y, Kacimi B. A review of analytical models to describe pull-out behavior – fiber/matrix adhesion. Compos Struct 2018;201:791–815. doi:10.1016/j.compstruct.2018.06.091.
[3] Banholzer B, Brameshuber W, Jung W. Analytical evaluation of pull-out tests-the inverse problem. Cem Concr Compos 2006;28:564–71. doi:10.1016/j.cemconcomp.2006.02.015.
[4] Ho H, Drzal LT. Evaluation of interfacial mechanical properties of fiber reinforced composites using the microindentation method. Compos Part A Appl Sci Manuf 1996;27:961–71. doi:10.1016/1359-835X(96)84802-0.
[5] Chen Dd-H, Nisitani H. Singular stress field near the corner of jointed dissimilar materials. J Appl Mech Trans ASME 1993;60:607–13. doi:10.1115/1.2900847.
[6] Chen Dd-H, Nisitani H. Singular stress field in two bonded wedges. Trans Japan Soc Mech Eng Ser A 1992;58:457–64. doi:10.1299/kikaia.58.457.
[7] Noda N-A, Li R, Miyazaki T, Takaki R, Sano Y. Convenient adhesive strength evaluation method in terms of the intensity of singular stress field. Int J Comput Methods 2019;16. doi:10.1142/S0219876218500858.
[8] Scheer RJ, Nairn JA. A comparison of several fracture mechanics methods for measuring interfacial toughness with microbond tests. J Adhes 1995;53:45–68. doi:10.1080/00218469508014371.
[9] Pisanova E, Zhandarov S, Mäder E, Ahmad I, Young RJ. Three techniques of interfacial bond strength estimation from direct observation of crack initiation and propagation in polymer-fibre systems. Compos Part A Appl Sci Manuf 2001;32:435–43. doi:10.1016/S1359-835X(00)00054-3.
[10] Zhandarov S, Mäder E. Characterization of fiber/matrix interface strength: applicability of different tests, approaches and parameters. Compos Sci Technol 2005;65:149–60. doi:10.1016/j.compscitech.2004.07.003.
[11] Marotzke C, Qiao L. Interfacial crack propagation arising in single-fiber pull-out tests. Compos Sci Technol 1997;57:887–97. doi:10.1016/S0266-3538(96)00179-0.
[12] Wang C. Fracture mechanics of single-fibre pull-out test. J Mater Sci 1997;32:483–90. doi:10.1023/A:1018534323464.
[13] Tsai K-H, Kim K-S. The micromechanics of fiber pull-out. J Mech Phys Solids 1996;44:1147–59. doi:10.1016/0022-5096(96)00019-1.
[14] Atkinson C, Avila J, Betz E, Smelser RE. The rod pull out problem, theory and experiment. J Mech Phys Solids 1982;30:97–120. doi:10.1016/0022-5096(82)90019-9.
[15] Goda K. Semi-discretization analysis for the shear-lag model with a viscoelastic matrix and its application to creep-rupture simulation using the bis method. Nihon Kikai Gakkai Ronbunshu. A Hen/Trans Japan Soc Mech Eng Part A 2000;66:480–8. doi:10.1299/kikaia.66.480.

[16] Hedgepeth JM, Van Dyke P. Local stress concentrations in imperfect filamentary composite materials. J Compos Mater 1967;1:294–309. doi:10.1177/002199836700100305.
[17] Batdorf SB. Note on shear interaction between two fibers. Eng Fract Mech 1983;18:1207–10. doi:10.1016/0013-7944(83)90014-0.
[18] Hutchinson JW, Jensen HM. Models of fiber debonding and pullout in brittle composites with friction. Mech Mater 1990;9:139–63. doi:10.1016/0167-6636(90)90037-G.
[19] Budiansky B, Evans AG, Hutchinson JW. Fiber-matrix debonding effects oncracking in aligned fiber ceramic composites. Int J Solids Struct 1995;32:315–28. doi:10.1016/0020-7683(94)00154-O.
[20] Povirk GL, Needleman A. Finite element simulations of fiber pull-out. J Eng Mater Technol Trans ASME 1993;115:286–91. doi:10.1115/1.2904220.
[21] Noda N-A, Miyazaki T, Uchikoba T, Li R, Sano Y, Takase Y. Convenient debonding strength evaluation based on the intensity of singular stress for adhesive joints. J Japan Inst Electron Packag 2014;17:132–42. doi:10.5104/jiep.17.132.
[22] Suzuki Y. Adhesive tensile strength of scarf and butt joints of steel plates (Relation between adhesive layer thicknesses and adhesive strengths of joints). JSME Int J 1987;30:1042–51. doi:10.1299/jsme1987.30.1042.
[23] Noda N-A, Miyazaki T, Li R, Uchikoba T, Sano Y, Takase Y. Debonding strength evaluation in terms of the intensity of singular stress at the interface corner with and without fictitious crack. Int J Adhes Adhes 2015;61:46–64. doi:10.1016/j.ijadhadh.2015.04.005.
[24] Miyazaki T, Noda N-A, Ren F, Wang Z, Sano Y, Iida K. Analysis of intensity of singular stress field for bonded cylinder and bonded pipe in comparison with bonded plate. Int J Adhes Adhes 2017;77:118–37. doi:10.1016/j.ijadhadh.2017.03.019.
[25] Noda N-A, Ren F, Takaki R, Wang Z, Oda K, Miyazaki T, et al. Intensity of singular stress field over the entire bond line thickness range useful for evaluating the adhesive strength for plate and cylinder butt joints. Int J Adhes Adhes 2018;85:234–50. doi:10.1016/j.ijadhadh.2018.05.013.
[26] Miyazaki T, Noda N-A, Wang Z, Sano Y. Analysis of intensity of singular stress field for bonded cylinder in comparison with bonded plate. Trans JSME (in Japanese) 2015;81 15-00210-15–00210. doi:10.1299/transjsme.15-00210.
[27] Noda N-A, Fei REN, Takaki R, Tsuboi K, Sano Y, Takase Y, et al. Validity of the adhesive strength evaluation method based on the intensity of singular stress field in two-dimensional modelling. J Japan Inst Electron Packag 2018;21:299–310. doi:10.5104/jiep.21.299.
[28] Noda N-A, Chen D, Takaki R, Inoue A, Zhang G, Sano Y. Intensity of singular stress fields of an embedded fiber under pull-out force. Zair Soc Mater Sci Japan 2018;67:1073–9. doi:10.2472/jsms.67.1073.
[29] Zhang Y, Noda N-A, Wu P, Duan M. International Journal of Adhesion & Adhesives a mesh-independent technique to evaluate stress singularities in adhesive joints. Int J Adhes Adhes 2015;57:105–17 the corrigendum of authorship is published in Int J Adhes Adhes 2015;60:130. doi:10.1016/j.ijadhadh.2014.12.003.
[30] Oda K, Kamisugi K, Noda NA. Analysis of stress intensity factor for interface cracks based on proportional method. Nihon Kikai Gakkai Ronbunshu. A Hen/Trans Japan Soc Mech Eng Part A 2009;75:476–82. doi:10.1299/kikaia.75.476.
[31] Nisitani H, Teranishi T. Highly accurate values of K_I and K_{II} of axially symmetrical cracked body subjected to tension obtained by FEM. Struct Mater 2000;6:461–9.
[32] Nisitani H, Teranishi T. KI of a circumferential crack emanating from an ellipsoidal cavity obtained by the crack tip stress method in FEM. Eng Fract Mech 2004;71:579–85. doi:10.1016/S0013-7944(03)00035-3.
[33] Miyazaki T. Proposal of a convenient and accurate method for evaluation of debonding strength. Trans Soc Automot Eng Japan 2014;45:895–901. doi:10.11351/jsaeronbun.45.895.
[34] Miyazaki T, Noda N-A, Sano Y. A precise and efficient analytical method to obtain two distinct intensities of singular stress fields for single lap joint. J Japan Inst Electron Packag 2018;21:166–77. doi:10.5104/jiep.21.166.
[35] Miyazaki T, Noda N-A. Evaluation of debonding strength of single lap joint by the intensity of singular stress field. J. Phys. Conf. Ser. 2017;842. doi:10.1088/1742-6596/842/1/012078.
[36] Noda N-A, Shirao R, Li J, Sugimoto J-S. Intensity of singular stress fields causing interfacial debonding at the end of a fiber under pullout force and transverse tension. Int J Solids Struct 2007;44:4472–91. doi:10.1016/j.ijsolstr.2006.11.034.
[37] Noda N-A, Wang Q, Uemura Y, Kawashima Y. Singular integral equation method in the analysis of interaction between rectangular inclusions. JSME Int J Ser A Mech Mater Eng 1998;41:303–8.
[38] Noda N-A, Takase Y, Iizuka T. Generalized stress intensity factors at the fiber end in fiber reinforced plastics. Nihon Kikai Gakkai Ronbunshu. A Hen/Trans Japan Soc Mech Eng Part A 2005;71:1132–9.
[39] Suga T, Elssner G, Schmauder S. Composite parameters and mechanical compatibility of material joints. J Compos Mater 1988;22:917–34. doi:10.1177/002199838802201002.
[40] Yuuki R. Mechanics of interface. 1993.
[41] Dundurs J. Effect of elastic constants on stress in a composite under plane deformation. J Compos Mater 1967;1:310–22. doi:10.1177/002199836700100306.
[42] Chen D-H, Nisitani H. Analysis of intensity of singular stress field at fiber end (2nd report, results of calculation). In: Trans Japan Soc Mech Eng Ser A, 58; 1992. p. 2153–8. doi:10.1299/kikaia.58.2153.
[43] Noda N-A, Chen X, Sano Y, Wahab MA, Maruyama H, Fujisawa R, et al. Effect of pitch difference between the bolt-nut connections upon the anti-loosening performance and fatigue life. Mater Des 2016;96:476–89. doi:10.1016/j.matdes.2016.01.128.
[44] Noda N-A, Takaki R, Shen Y, Inoue A, Sano Y, Akagi D, et al. Strain rate concentration factor for flat notched specimen to predict impact strength for polymeric materials. Mech Mater 2019;131:141–57. doi:10.1016/j.mechmat.2019.01.011.
[45] Wang Z, Noda N-A, Ueno M, Sano Y. Optimum design of ceramic spray coating evaluated in terms of intensity of singular stress field. Steel Res Int 2017;88. doi:10.1002/srin.201600353.
[46] Stern M, Soni ML. On the computation of stress intensities at fixed-free corners. Int J Solids Struct 1976;12:331–7. doi:10.1016/0020-7683(76)90023-8.
[47] Freund LB. Axial force needed to slide a circular fiber along a hole in an elastic material and implications for fiber pull-out. Eur J Mech A/Solids 1992;11:1–19.
[48] Hann LP, Hirt DE. Simulating the microbond technique with macrodroplets. Compos Sci Technol 1995;54:423–30. doi:10.1016/0266-3538(95)00080-1.
[49] Ash JT, Cross WM, Svalstad D, Kellar JJ, Kjerengtroen L. Finite element evaluation of the microbond test: meniscus effect, interphase region, and vise angle. Compos Sci Technol 2003;63:641–51. doi:10.1016/S0266-3538(02)00256-7.
[50] Zhang X, Liu H-Y, Mai Y-W. Effects of fibre debonding and sliding on the fracture behaviour of fibre-reinforced composites. Compos Part A Appl Sci Manuf 2004;35:1313–23. doi:10.1016/j.compositesa.2004.03.011.
[51] Brito-Santana H, Thiesen JLM, de Medeiros R, Ferreira AJM, Rodríguez-Ramos R, Tita V. Multiscale analysis for predicting the constitutive tensor effective coefficients of layered composites with micro and macro failures. Appl Math Model 2019;75:250–66. doi:10.1016/j.apm.2019.05.031.
[52] Ranjbarian M, Mechtcherine V, Zhang Z, Curosu I, Storm J, Kaliske M. Locking front model for pull-out behaviour of PVA microfibre embedded in cementitious matrix. Cem Concr Compos 2019;103:318–30. doi:10.1016/j.cemconcomp.2019.04.031.
[53] Storm J, Ranjbarian M, Mechtcherine V, Scheffler C, Kaliske M. Modelling of fibre-reinforced composites via fibre super-elements. Theor Appl Fract Mech 2019;103. doi:10.1016/j.tafmec.2019.102294.
[54] Vázquez-Rodríguez JM, Flores-Johnson EA, Herrera-Franco PJ, Gonzalez-Chi PI. Photoelastic and numerical analyses of the stress distribution around a fiber in a pull-out test for a thermoplastic fiber/epoxy resin composite. Polym Compos 2018;39:E2397–406. doi:10.1002/pc.24709.
[55] Frikha M, Nouri H, Guessasma S, Roger F, Bradai C. Interfacial behaviour from pull-out tests of steel and aluminium fibres in unsaturated polyester matrix. J Mater Sci 2017;52:13829–40. doi:10.1007/s10853-017-1486-7.
[56] Serra J, Bouvet C, Castanié B, Petiot C. Experimental and numerical analysis of carbon fiber reinforced polymer notched coupons under tensile loading. Compos Struct 2017;181:145–57. doi:10.1016/j.compstruct.2017.08.090.
[57] Poniznik Z, Nowak Z, Basista M. Numerical modeling of deformation and fracture of reinforcing fibers in ceramic-metal composites. Int J Damage Mech 2017;26:711–34. doi:10.1177/1056789515611945.
[58] Kundalwal SI, Kumar S. Multiscale modeling of stress transfer in continuous microscale fiber reinforced composites with nano-engineered interphase. Mech Mater 2016;102:117–31. doi:10.1016/j.mechmat.2016.09.002.
[59] Paul BK, Ahmed K, Vigneswaran D, Ahmed F, Roy S, Abbott D. Quasi-photonic crystal fiber-based spectroscopic chemical sensor in the terahertz spectrum: design and analysis. IEEE Sens J 2018;18:9948–54. doi:10.1109/JSEN.2018.2872892.
[60] Jabin MA, Ahmed K, Rana MJ, Paul BK, Islam M, Vigneswaran D, et al. Surface plasmon resonance based titanium coated biosensor for cancer cell detection. IEEE Photonics J 2019;11. doi:10.1109/JPHOT.2019.2924825.
[61] Ahmed K, Haque MJ, Jabin MA, Paul BK, Amiri IS, Yupapin P. Tetra-core surface plasmon resonance based biosensor for alcohol sensing. Phys B Condens Matter 2019;570:48–52. doi:10.1016/j.physb.2019.05.047.
[62] Ahmed K, Paul BK, Jabin MA, Biswas B. FEM analysis of birefringence, dispersion and nonlinearity of graphene coated photonic crystal fiber. Ceram Int 2019;45:15343–7. doi:10.1016/j.ceramint.2019.05.027.
[63] Paul BK, Chakma S, Khalek MA, Ahmed K. Silicon nano crystal filled ellipse core based quasi photonic crystal fiber with birefringence and very high nonlinearity. Chinese J Phys 2018;56:2782–8. doi:10.1016/j.cjph.2018.09.030.
[64] Miyazaki T, Noda N-A, Li R, Uchikoba T, Sano Y. Debonding criterion for single lap joints from the intensity of singular stress field. J Japan Inst Electron Packag 2013;16:143–51. doi:10.5104/jiep.16.143.
[65] Bogy DB. Edge-bonded dissimilar orthogonal elastic wedges under normal and shear loading. J Appl Mech Trans ASME 1964;35:460–6. doi:10.1115/1.3601236.
[66] Bogy DB. Two edge-bonded elastic wedges of different materials and wedge angles under surface tractions. J Appl Mech Trans ASME 1971;38:377–86. doi:10.1115/1.3408786.
[67] Carpenter WC. Mode I and mode II stress intensities for plates with cracks of finite opening. Int J Fract 1984;26:201–14. doi:10.1007/BF01140628.
[68] Carpenter WC, Byers C. A path independent integral for computing stress intensities for V-notched cracks in a bi-material. Int J Fract 1987;35:245–68. doi:10.1007/BF00276356.
[69] Gao S-L, Mäder E, Zhandarov SF. Carbon fibers and composites with epoxy resins: topography, fractography and interphases. Carbon N Y 2004;42:515–29. doi:10.1016/j.carbon.2003.12.085.
[70] Sinclair GB, Okajima M, Griffin JH. Path independent integrals for computing stress intensity factors at sharp notches in elastic plates. Int J Numer Method Eng 1984;20:999–1008. doi:10.1002/nme.1620200603.
[71] Williams ML. The stresses around a fault or crack in dissimilar media. Bull Seismol Soc Am 1959;49:199–204.
[72] Stern M, Becker EB, Dunham RS. A contour integral computation of mixed-mode stress intensity factors. Int J Fract 1976;12:359–68. doi:10.1007/BF00032831.